

# High order discontinuous Galerkin simulation of hypersonic shock-boundary layer interaction using subcell limiting approach

Vachan D. Potluri<sup>\*1</sup>, Bhalchandra P. Puranik<sup>1</sup>, and Kowsik V. R. Bod<sup>2</sup>

<sup>1</sup>Department of Mechanical Engineering, Indian Institute of Technology, Bombay

<sup>2</sup>Department of Aerospace Engineering, Indian Institute of Technology, Bombay

## Abstract

Numerical simulation of shock-boundary layer interactions in the hypersonic regime has for long been a challenge, plagued by high sensitivity of the surface predictions to grid and numerical details. In the course of developing adaptive high order methods to mitigate this issue, discontinuous Galerkin method has emerged as a promising alternative to the conventionally used finite volume method. However, till date, among the reported finite element method-based simulations of these flows, only a few have presented high order simulations using a higher than linear basis. In this work, a subcell limiting technique devised for the compressible Navier-Stokes equations is extended for use in the hypersonic regime. The proposed extension is tested by performing simulations of several shock-boundary layer interaction cases in the freestream Mach number range 6 to 14 using a quadratic basis. For a set of cases at Mach 6, grid converged simulations are presented that agree reasonably well with experimental data and other numerical solutions. More importantly, simulations of a Mach 11 case that are performed using two different flux schemes are shown to yield nearly identical predictions of the surface pressure and heat transfer, suggesting that high order solutions can reduce the sensitivity of numerical predictions to the computational details. Grid convergence studies of two cases at Mach numbers 11 and 14 led to observing large scale oscillations in the separation bubble in finer grid simulations, suggesting that explicit time integration may not always be suitable for high order computation of hypersonic separated flows at very high Mach numbers.

**Keywords** Hypersonic flow, shock-boundary layer interaction, discontinuous Galerkin method, high order simulation

## 1 Introduction

Robust numerical simulation of hypersonic flows, specifically slender body flows which involve strong viscous-inviscid interaction, is still a subject of active research. In the past few decades, Finite Volume Method (FVM) has been predominantly used to simulate these flows [1, 2]. One of the major issues in computation of such hypersonic flows is the high sensitivity of the calculated surface heat transfer to the grid distribution and the details of the computational method used, motivating the development of adaptive high order numerical algorithms for a possible remedy [3, 4]. While efforts are being made to solve this issue in the Finite Volume (FV) approach using techniques like adaptive mesh refinement [5–7] and high order discretisation [8, 9], Finite Element Method (FEM) based algorithms, and particularly the Discontinuous Galerkin (DG) method [10], have emerged as one reliable alternative to FVM. The DG method has garnered significant interest in the past two decades since it (i) can perform arbitrarily high order accurate computations without much increase in algorithmic complexity, (ii) conveniently handles complex and/or curved meshes, and (iii) has high suitability to  $hp$ -adaptivity and parallelisation owing to its compact cell-local interpolation [11, 12]. These favourable numerical attributes make it a worthy alternative to FVM and one of the potential routes to solve the aforementioned issue.

However, one significant challenge in the development of a DG algorithm for hypersonic flows is the shock stabilisation procedure. To simulate discontinuous flow features stably without oscillations, a DG method requires appropriate measures akin to finite volume slope/flux limiters and non-oscillatory reconstruction procedures. Entropy-stable DG discretisations [13, 14], along with entropy-stable boundary conditions [15, 16] are shown to provide stable solutions on their own without any additional stabilisation measures for supersonic shocked flows,

---

<sup>\*</sup>vachanpotluri@iitb.ac.in

and even for flow with stronger shocks when used together with  $hp$ -adaptation. Nevertheless, the procedure for shock stabilisation becomes increasingly complex in hypersonic flows, because the simultaneous existence of high gradients in both shocks and shear layers, together with strong viscous-inviscid coupling offers a difficult challenge for DG algorithms. Furthermore, standard hypersonic experiments that are often used for validation are numerically replicated with isothermal wall boundary condition, which cannot be accommodated in the existing entropy-stable boundary condition formulation [15].

In the past decade, a number of efforts were made to simulate hypersonic flows using DG and other FEM-based techniques. Kirk & Carey [17] developed a Streamwise Upwind Petrov Galerkin (SUPG) method to simulate laminar perfect gas hypersonic flows. The SUPG method adds an upwind bias to the finite element basis functions for stable discretisation of the convective term. An artificial viscosity based limiting approach is used to capture the discontinuities. Subsequently, this method was also extended to simulate turbulent flows in thermochemical nonequilibrium by Kirk *et al.* [18]. In a separate work, Holst *et al.* [19] have also demonstrated the validation of an SUPG method combined with artificial viscosity limiting for laminar perfect gas hypersonic flows. Recently, Seguin *et al.* [20] have developed an edge-based FEM solver for laminar hypersonic flows in thermochemical nonequilibrium which uses linear basis functions and a Galerkin discretisation. Shock capturing is done using the standard MUSCL slope limiter approach. This solver was improved by Gao *et al.* [21], wherein an anisotropic mesh refinement algorithm was introduced and validated. Bhatia *et al.* [22] had developed an  $rp$ -adaptive DG method for simulation of laminar hypersonic flows in thermochemical nonequilibrium. In this algorithm, shock capturing is done by rearranging the computational mesh near the shock location and performing a first order simulation ( $p = 0$ ) in this region, while retaining the high order simulation elsewhere. Barter & Darmofal [23] have proposed a smooth PDE-based artificial viscosity DG limiter for laminar perfect gas hypersonic flows. The development of a smooth artificial viscosity limiter was motivated by the observation that elementwise constant artificial viscosity introduces oscillations near shocks due to sudden changes in the solution gradients. Significant improvements in a hypersonic blunt body simulation were demonstrated using this novel approach. Subsequently, Burgess & Mavriplis [24] used this smooth artificial viscosity approach to develop an  $hp$ -adaptive two-dimensional DG solver for laminar perfect gas hypersonic flows. This solver was later extended to handle three-dimensional mixed element meshes by Brazell & Mavriplis [25]. Recently Ching *et al.* [26] proposed a modification to this smooth artificial viscosity approach, and demonstrated that as the basis polynomial order is increased, blunt body heat transfer results become less sensitive to the grid skewness and the computed heat transfer on a double cone configuration becomes less sensitive to the numerical method. This recent finding suggests that the DG method holds promise to deal with the sensitivity issues mentioned earlier.

Many FEM-based works in the literature use a linear polynomial basis for simulation [17–22], with a few efforts [23–26] presenting solutions that use higher than linear basis, of which only a fraction [26] demonstrate their use in hypersonic shock-boundary layer interaction (SBLI) configurations. In the present work, a subcell limiting strategy for the compressible Navier-Stokes (NS) equations [27] is extended for application to the hypersonic flow regime. Third (and, in some cases, higher) order simulations of various hypersonic SBLI flows are presented to assess the performance of the proposed extension.

This article is organised as follows. Section 2 describes the governing equations for laminar perfect gas compressible flow. Section 3 describes the limiter algorithm in brief along with the proposed extension to make it applicable in the hypersonic regime. Verification and validation of the algorithm is presented in Section 4, along with highlighting its limitations. Finally, Section 5 concludes the work and provides some suggestions for related future work.

## 2 Physical modelling and governing equations

This work is concerned with the three-dimensional compressible NS equations, given by

$$\frac{\partial \mathbf{U}}{\partial t} + \sum_{i=1}^3 \left[ \frac{\partial \mathcal{F}_{ai}}{\partial x_i} + \frac{\partial \mathcal{F}_{di}}{\partial x_i} \right] = \mathbf{0},$$

where  $\mathbf{U} := [\rho \rho u_1 \rho u_2 \rho u_3 \rho E]^T$  is the state vector,  $\mathcal{F}_{ai}$  and  $\mathcal{F}_{di}$  are respectively the advective and diffusive fluxes in the  $i$ -th direction, given by

$$\mathcal{F}_{ai}(\mathbf{U}) := \begin{bmatrix} \rho u_i \\ \rho u_1 u_i \\ \rho u_2 u_i \\ \rho u_3 u_i \\ \rho E u_i \end{bmatrix} + p \begin{bmatrix} 0 \\ \delta_{1i} \\ \delta_{2i} \\ \delta_{3i} \\ u_i \end{bmatrix} \quad \text{and} \quad \mathcal{F}_{di}(\mathbf{U}, \nabla \mathbf{U}) := - \begin{bmatrix} 0 \\ \tau_{1i} \\ \tau_{2i} \\ \tau_{3i} \\ \sum_{j=1}^3 \tau_{ij} u_j - q''_i \end{bmatrix} \quad (i = 1, 2, 3).$$

Here,  $\rho$  and  $p$  represent density and pressure respectively,  $\mathbf{u} = [u_1, u_2, u_3]^T$  is the velocity vector, and  $\delta_{ij}$  is the Kronecker delta. Furthermore,  $E := e + (\mathbf{u} \cdot \mathbf{u})/2$  and  $e := p/((\gamma - 1)\rho)$  are the specific total energy and the specific thermal energy of a calorically perfect gas with specific heat ratio  $\gamma$ . Components of the shear stress tensor and the heat flux vector are respectively given by

$$\begin{aligned} \tau_{ij} &= \mu \left( \frac{\partial u_i}{\partial x_j} + \frac{\partial u_j}{\partial x_i} \right) - \frac{2\mu}{3} \delta_{ij} \sum_{l=1}^3 \frac{\partial u_l}{\partial x_l} \quad (i, j = 1, 2, 3), \\ q''_i &= -k \frac{\partial T}{\partial x_i} \quad (i = 1, 2, 3), \end{aligned}$$

where  $\mu$  is the dynamic viscosity,  $k$  is the thermal conductivity, and  $T$  is the temperature; which is related to density and pressure through the perfect gas equation of state  $p = \rho RT$  ( $R$  being the specific gas constant). The coefficient of viscosity is modelled using the Sutherland's law

$$\mu = \mu_0 \left( \frac{T}{T_0} \right)^{3/2} \frac{T_0 + S}{T + S}$$

and the thermal conductivity is obtained by assuming a constant Prandtl number  $\text{Pr} := \mu c_p/k$ , where  $c_p = \gamma R/(\gamma - 1)$  is the specific heat at constant pressure. The gases used for simulation in this work are air and nitrogen for which the Sutherland's constants are given in Table 1.

**Table 1:** Sutherland's constants and Prandtl number for air and nitrogen [28].

Gas	$\mu_0$ (N s m <sup>-2</sup> )	$T_0$ (K)	$S$ (K)	Pr
Air	$1.716 \times 10^{-5}$	273	111	0.69
N <sub>2</sub>	$1.663 \times 10^{-5}$	273	107	0.69

### 3 Numerical method

#### 3.1 One-dimensional Euler equations

The subcell limiter algorithm proposed by Hennemann *et al.* [27] for the Euler equations is described here in brief in a one-dimensional setting. The one-dimensional Euler equations read as

$$\frac{\partial \mathbf{U}}{\partial t} + \frac{\partial \mathcal{F}_{a1}}{\partial x_1} = \mathbf{0} \quad (t \geq 0, x_1 \in \Omega). \quad (1)$$

For simplicity, the subscripts “a” and “1” are dropped in this section. The computational domain  $\Omega$  is partitioned into non-overlapping one-dimensional elements. Consider the restriction of Eq. (1) to a representative element  $\Omega_e := [a, b]$ , which is being mapped to the reference element  $\Omega_{\text{ref}} := [0, 1]$  using the linear mapping  $\xi \xrightarrow{\mathcal{M}} x$ :

$$\begin{aligned} \mathcal{M}^{-1}(x) &= \xi = \frac{x - a}{b - a} \quad (x \in \Omega_e), \\ J \frac{\partial \mathbf{U}}{\partial t} + \frac{\partial \mathbf{F}}{\partial \xi} &= \mathbf{0} \quad (t \geq 0, \xi \in \Omega_{\text{ref}}), \end{aligned}$$

where  $\mathbf{U}(\xi, t) := \mathcal{U}(x, t)$ ,  $\mathbf{F}(\mathbf{U}) := \mathcal{F}(\mathbf{U})$  are the conservative state and flux in the reference space, and  $J := d\mathbf{M}/d\xi = (b - a)$  is the Jacobian of the mapping.  $\mathbf{U}$  and  $\mathbf{F}$  are approximated to lie in a linear polynomial space of  $N$ -th degree polynomials

$$\mathbf{U}(\xi, t) \approx \sum_{i=0}^N \mathbf{U}_i(t) \ell_i(\xi), \quad \mathbf{F}(\xi, t) \approx \sum_{i=0}^N \mathbf{F}(\mathbf{U}_i(t)) \ell_i(\xi),$$

where  $\{\ell_i(\xi)\}_{i=0}^N$  are the basis functions of the polynomial space, and  $\{\mathbf{U}_i\}_{i=0}^N$  are the nodal values of the solution. These basis functions are the Lagrange functions constructed using the  $(N + 1)$  Gauss-Lobatto (GL) points  $\{\xi_i\}_{i=0}^N$  (termed “nodes”). The error in this approximation is minimised using the Galerkin approach in a strong sense with the test functions  $\{\ell_j\}_{j=0}^N$ :

$$\int_0^1 \ell_j J \frac{\partial \mathbf{U}}{\partial t} d\xi + \int_0^1 \ell_j \frac{\partial \mathbf{F}}{\partial \xi} d\xi + [\ell_j (\mathbf{F}^* - \mathbf{F})]_{\xi=0}^{1} = \mathbf{0} \quad (j = 0, 1, \dots, N), \quad (2)$$

where  $\mathbf{F}^*$  is the numerical flux function introduced at the element boundaries to ensure conservation. Eq. (2) can be simplified by introducing the **mass**, **stiffness** and **boundary evaluation** matrices  $\underline{M}$ ,  $\underline{S}$  and  $\underline{B}$ :

$$\begin{aligned} & \sum_{j=0}^N M_{ij} J \dot{\mathbf{U}}_j + S_{ij} \mathbf{F}_j + B_{ij} (\mathbf{F}_j^* - \mathbf{F}_j) = 0 \quad (i = 0, 1, \dots, N), \\ & M_{ij} := \int_0^1 \ell_i \ell_j d\xi \quad (i, j = 0, 1, \dots, N), \\ & S_{ij} := \int_0^1 \ell_i \frac{d\ell_j}{d\xi} d\xi \quad (i, j = 0, 1, \dots, N), \\ & \underline{B} := \text{diag}(-1, 0, \dots, 0, 1) \in \mathbb{R}^{(N+1)} \end{aligned} \quad (3)$$

where  $\mathbf{F}_j = \mathbf{F}(\mathbf{U}_j)$ , and  $\mathbf{F}_j^*$  is the inter-element numerical flux (non-zero only for  $j = 0$  and  $N$ ). Eq. (3) is a matrix representation of the strong Galerkin formulation (Eq. 2).

In the DG Spectral Element Method (DGSEM), co-located quadrature is used to evaluate elements of  $\underline{M}$  and  $\underline{S}$ . In this approach, the  $(N + 1)$  GL points  $\{\xi_i\}_{i=0}^N$  along with GL quadrature weights  $\{w_i\}_{i=0}^N$  are used for numerical quadrature of the integrals in Eq. (3). This simplifies the matrix element expressions, and also the strong form discretization as follows:

$$\begin{aligned} & \underline{M} = \text{diag}(w_0, w_1, \dots, w_N), \\ & \underline{S} = \underline{M} \underline{D}, \quad D_{ij} = \frac{d\ell_j}{d\xi}(\xi_i) \quad (i, j = 0, 1, \dots, N), \\ & -J \dot{\mathbf{U}}_i = \sum_{j=0}^N [D_{ij} \mathbf{F}_j] - \frac{\delta_{0i}}{w_0} (\mathbf{F}_0^* - \mathbf{F}_0) + \frac{\delta_{Ni}}{w_N} (\mathbf{F}_N^* - \mathbf{F}_N) := R_{\text{std}}(\mathbf{F})_i \quad (i = 0, 1, \dots, N), \end{aligned} \quad (4)$$

where  $\underline{D}$  is the **polynomial derivative** matrix. Eq. (4) is the standard DGSEM discretisation, and also defines  $R_{\text{std}}(\mathbf{F})_i$  which is the standard DGSEM residual due to the flux  $\mathbf{F}$  at node  $i$  (“std” abbreviates “standard”).

The use of co-located quadrature also gives summation-by-parts property to  $\underline{S}$  which allows writing the volumetric term of Eq. (4) as a flux difference [29]:

$$\sum_{j=0}^N D_{ij} \mathbf{F}_j = \frac{\widehat{\mathbf{F}}_{i+1} - \widehat{\mathbf{F}}_i}{w_i} \quad (i = 0, 1, \dots, N). \quad (5)$$

Here  $\{\widehat{\mathbf{F}}_i\}_{i=0}^{N+1}$  are the corresponding consistent volumetric fluxes defined on the **flux points**  $\{\widehat{\xi}_i\}_{i=0}^{N+1}$ . These flux points are related to the GL points through the GL weights as follows.

$$\widehat{\xi}_0 = \xi_0; \quad \widehat{\xi}_{N+1} = \xi_N; \quad \widehat{\xi}_{i+1} - \widehat{\xi}_i = w_i \quad (i = 0, 1, \dots, N)$$

This results in a decomposition of every element into subcells of widths  $\{w_i\}_{i=0}^N$  in the reference space. A visual representation is shown in Fig. 1. With the help of Fig. 1, one can see that Eq. (5) provides an interpretation of the standard DGSEM discretisation as a subcell finite volume discretisation with a flux reconstruction.

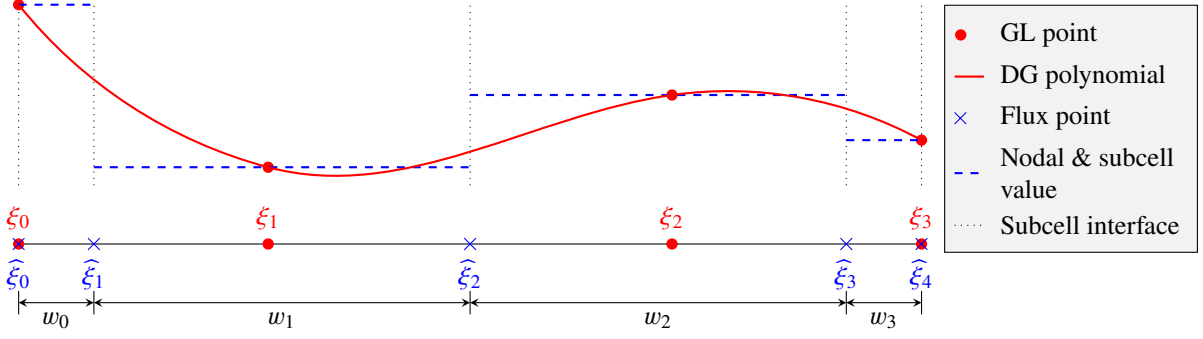


**Figure 1:** Equivalent subcell decomposition for a one-dimensional cubic DGSEM element ( $N = 3$ ).

While the relation between volumetric fluxes ( $\{\widehat{\mathbf{F}}_i\}_{i=0}^{N+1}$ ) and nodal fluxes ( $\{\mathbf{F}_j\}_{j=0}^N$ ) is given in [29], Carpenter *et al.* [30], extended the work of Fisher & Carpenter [31] for Euler equations. This lead to the development of **split-form** DGSEM, as studied by Gassner *et al.* [32], in which the volumetric fluxes are constructed independent of the nodal fluxes using a **volumetric two-point flux function** denoted by  $\mathbf{F}^\#(\bullet, \bullet)$ :

$$\begin{aligned}\widehat{\mathbf{F}}_0^{\text{HO}} &\approx \mathbf{F}_0, \quad \widehat{\mathbf{F}}_{N+1}^{\text{HO}} \approx \mathbf{F}_N, \\ \widehat{\mathbf{F}}_i^{\text{HO}} &\approx \sum_{j=i}^N \sum_{k=0}^{i-1} 2w_k D_{kj} \mathbf{F}^\#(\mathbf{U}_k, \mathbf{U}_j) \quad (i = 1, 2, \dots, N),\end{aligned}\quad (6)$$

where HO stands for ‘‘high order’’ to denote that this choice of flux retains the high order accuracy of the standard discretisation provided  $\mathbf{F}^\#(\bullet, \bullet)$  satisfies some basic properties. This split-form discretization has anti-aliasing properties and, depending on the choice of  $\mathbf{F}^\#$ , can also have entropy or kinetic energy stability in smooth regions [33]. Substituting Eqs. (5) and (6) in Eq. (4), the split-form DGSEM discretization can be written as

$$-J\dot{\mathbf{U}}_i = 2 \sum_{j=0}^N D_{ij} \mathbf{F}^\#(\mathbf{U}_i, \mathbf{U}_j) - \frac{\delta_{0i}}{w_0} (\mathbf{F}_0^* - \mathbf{F}_0) + \frac{\delta_{Ni}}{w_N} (\mathbf{F}_N^* - \mathbf{F}_N) := R_{\text{sf}}^{\text{HO}}(\mathbf{F})_i \quad (i = 0, 1, \dots, N), \quad (7)$$

where the subscript ‘‘sf’’ abbreviates ‘‘split-form’’ and  $R_{\text{sf}}^{\text{HO}}(\mathbf{F})_i$  is the high-order split-form DGSEM residual at node  $i$  due to the flux  $\mathbf{F}$ .

Hennemann *et al.* [27] proposed a limiting technique where the split-form high order DGSEM discretisation is blended with a low order discretisation. Since the introduction to flux points and volumetric fluxes provides a natural subcell decomposition of the finite element (see Fig. 1), the ‘‘low order’’ scheme was constructed by defining the volumetric fluxes using the left and right subcell values as follows.

$$\begin{aligned}\widehat{\mathbf{F}}_0^{\text{LO}} &\approx \mathbf{F}_0, \quad \widehat{\mathbf{F}}_{N+1}^{\text{LO}} \approx \mathbf{F}_N, \\ \widehat{\mathbf{F}}_i^{\text{LO}} &\approx \mathbf{F}^*(\mathbf{U}_{i-1}, \mathbf{U}_i) \quad (i = 1, 2, \dots, N)\end{aligned}\quad (8)$$

Substituting Eqs. (5) and (8) in the second term of Eq. (4) gives a low-order residual based on a first order subcell discretization

$$R_{\text{sc}}^{\text{LO}}(\mathbf{F})_i := \frac{\widehat{\mathbf{F}}_{i+1}^{\text{LO}} - \widehat{\mathbf{F}}_i^{\text{LO}}}{w_i} - \frac{\delta_{0i}}{w_0} (\mathbf{F}_0^* - \mathbf{F}_0) + \frac{\delta_{Ni}}{w_N} (\mathbf{F}_N^* - \mathbf{F}_N) \quad (i = 0, 1, \dots, N) \quad (9)$$

where the subscript ‘‘sc’’ abbreviates ‘‘subcell’’. Limiting is achieved by blending the low order discretisation (Eq. 9) with the high order discretisation (Eq. 7) using a blender  $\alpha$ .

$$J\dot{\mathbf{U}}_i + (1 - \alpha)R_{\text{sf}}^{\text{HO}}(\mathbf{F})_i + \alpha R_{\text{sc}}^{\text{LO}}(\mathbf{F})_i = 0 \quad (i = 0, 1, \dots, N) \quad (10)$$

### 3.1.1 Calculation of the blender

The blending coefficient  $\alpha$  is calculated by estimating the relative energy contained in the high order mode(s) of a certain physical quantity, say  $\epsilon$ . Following Hennemann *et al.* [27], the product of density and pressure ( $\epsilon = \rho p$ )

is used for trouble detection in this work. To this end,  $\epsilon$  is expressed in modal representation with the Legendre polynomials  $\{P_j(\xi)\}_{j=0}^N$  as the basis functions:

$$\epsilon(\xi) = \sum_{i=0}^N m_i P_i(\xi).$$

While Persson & Peraire [34] suggest using the relative energy in highest mode as the energy indicator (Eq. 11), Hennemann *et al.* [27] suggest a modification to (Eq. 12) where the next highest mode is also considered.

$$\Xi_P = \frac{m_N^2}{\sum_{i=0}^N m_i^2} \quad (11)$$

$$\Xi_H = \max \left\{ \frac{m_N^2}{\sum_{i=0}^N m_i^2}, \frac{m_{N-1}^2}{\sum_{i=0}^{N-1} m_i^2} \right\} \quad (12)$$

In this work,  $\Xi_P$  is used whenever  $N \leq 2$ . In cases with  $N > 2$ , it is observed that  $\Xi_P$  suffices for stable computation of supersonic cases, and  $\Xi_H$  is employed only for hypersonic cases. The relative energy so calculated is compared with a threshold ( $\mathbb{T}$ ) before finally calculating the blender value as follows.

$$\begin{aligned} \mathbb{T}(N) &= 0.5 \times 10^{-1.8(N+1)^{0.25}}, \\ \alpha'' &= \frac{1}{1 + \exp[-s(\frac{\Xi}{\mathbb{T}} - 1)]}, \quad s = 9.21024, \\ \alpha' &= \begin{cases} 0, & \text{if } \alpha'' < \alpha_{\min} \\ \alpha'', & \text{if } \alpha_{\min} < \alpha'' < \alpha_{\max} \\ \alpha_{\max} & \text{otherwise} \end{cases} \\ \alpha &= \max_{n \in \text{Neighbors}} (\alpha', 0.5\alpha'_n) \end{aligned}$$

In this work, while  $\alpha_{\min}$  is set to  $1 \times 10^{-3}$ ,  $\alpha_{\max}$  is set to 0.5 and 1 for supersonic and hypersonic cases respectively.

### 3.1.2 Choice of volume and surface fluxes

In this work, the Chandrashekhar volumetric flux [33] is used,

$$\mathbf{F}_{\text{Ch}}^\#(\mathbf{U}_a, \mathbf{U}_b) = \begin{bmatrix} \rho^{\ln \{\{u_1\}\}} \\ \rho^{\ln \{\{u_1\}\}^2 + \frac{\{\{\rho\}\}}{2\{\{\beta\}\}}} \\ \rho^{\ln \{\{u_1\}\} \{\{u_2\}\}} \\ \rho^{\ln \{\{u_1\}\} \{\{u_3\}\}} \\ \rho^{\ln \{\{u_1\}\} \left( \frac{1}{2\beta^{\ln(\gamma-1)}} + \frac{\{\{\rho\}\}}{2\rho^{\ln \{\{\beta\}\}}} + \sum_{i=1}^3 \left[ \{\{u_i\}\}^2 - \frac{1}{2} \{\{u_i^2\}\} \right] \right)} \end{bmatrix},$$

where  $\{\{x\}\} := (x_a + x_b)/2$ ,  $x^{\ln} := (x_a - x_b)/\ln(x_a/x_b)$  and  $\beta := \rho/2p$ . A numerically stable procedure to calculate the logarithmic averages is given in the appendix of [35]. A corresponding numerical surface flux  $\mathbf{F}^*$ , can be obtained by adding a stabilisation (dissipation) term to the volume flux. Here, the hybrid matrix based stabilisation [33] is used, which gives

$$\begin{aligned} \mathbf{F}_{\text{Ch}}^*(\mathbf{U}_a, \mathbf{U}_b) &= \mathbf{F}_{\text{Ch}}^\#(\mathbf{U}_a, \mathbf{U}_b) - \frac{1}{2} \mathbf{K} |\Lambda| \mathbf{K}^{-1} (\mathbf{U}_b - \mathbf{U}_a), \\ |\Lambda| &= \alpha |\Lambda|^{\text{Rus}} + (1 - \alpha) |\Lambda|^{\text{KES}}, \\ |\Lambda|^{\text{Rus}} &= (|\tilde{u}_1| + \tilde{a}) \mathbf{I}, \\ |\Lambda|^{\text{KES}} &= \text{diag}(|\tilde{u}_1| + \tilde{a}, |\tilde{u}_1|, |\tilde{u}_1|, |\tilde{u}_1|, |\tilde{u}_1| + \tilde{a}), \end{aligned}$$

where superscript  $\sim$  is used to denote Roe-averaged quantities,  $\mathbf{K}$  is the right eigenvector matrix of Roe-averaged state,  $\mathbf{I}$  is the identity matrix of size 5, “KES” stands for “kinetic energy stable”, and “Rus” abbreviates Rusanov.

A collection of other options for the volumetric fluxes along with their surface flux pairs is given in [32]. As regards the surface fluxes, it is also possible to use the standard numerical flux schemes (like HLLC, Roe, AUSM,

Rusanov etc.) independent to the choice of volume flux. Along with Chandrashekhar's surface flux, a hybrid Rusanov-HLLC flux scheme is also used in this work, which reads

$$\mathbf{F}_{\text{Rus-HLLC}}^* = \alpha_f \mathbf{F}_{\text{Rus}}^* + (1 - \alpha_f) \mathbf{F}_{\text{HLLC}}^*, \quad \alpha_f = \begin{cases} (\alpha_e + \alpha_n)/2 & \text{for internal cells,} \\ \alpha_e & \text{for boundary cells,} \end{cases}$$

where  $f$ ,  $e$  and  $n$  are used to denote a face, the element connected to the face, and the element's neighbour respectively.

### 3.2 Extension to Navier-Stokes equations

For simplicity, the extension will be described for the one-dimensional NS equations given by

$$\frac{\partial \mathbf{U}}{\partial t} + \frac{\partial \mathcal{F}_a}{\partial x} + \frac{\partial \mathcal{F}_d}{\partial x} = \mathbf{0} \quad (t \geq 0, x \in \Omega), \quad (13)$$

where the subscript '1' has been dropped for simplicity. The discretisation of the advection flux is kept unchanged and is given by Eq. (10).  $\nabla \mathbf{u}$  and  $\nabla T$  are additionally required to discretise the diffusive flux. In the BR1 approach (Bassi & Rebay [36]), these gradients are calculated by introducing the gradients of conservative variables as **auxiliary variables** to append the NS equation system. As a variant, Gassner *et al.* [37] suggested using entropy variable gradients as the auxiliary variables to retain the entropy stability property of the split-form DGSEM method. For brevity, the extension will be described using entropy variable gradients in this and the following sections. The use of conservative variable gradients can be similarly implemented.

The entropy variables, denoted by  $\mathbf{W}$ , for the NS equations are given by [38]

$$\mathbf{W} = \left[ \frac{\gamma - s}{\gamma - 1} - \beta \sum_{i=1}^3 u_i^2, 2\beta u_1, 2\beta u_2, 2\beta u_3, -2\beta \right]^T,$$

where  $s := (\ln p - \gamma \ln \rho)$  is the thermodynamic entropy and  $\beta := \rho/2p$  is a measure of the inverse of temperature. The gradients of these entropy variables, denoted by  $\mathcal{Z}$ , will be introduced as auxiliary variables to append the one-dimensional NS equations (Eq. 13).

$$\mathcal{Z} + \frac{\partial(-\mathbf{W})}{\partial x} = \mathbf{0} \quad (14a)$$

$$\frac{\partial \mathbf{U}}{\partial t} + \frac{\partial \mathcal{F}_a(\mathbf{U})}{\partial x} + \frac{\partial \mathcal{F}_d(\mathbf{U}, \mathcal{Z})}{\partial x} = \mathbf{0} \quad (14b)$$

Equation (14a) is solved (in the reference space) at every (sub-)time step using the standard DGSEM discretisation:

$$J\mathbf{Z}_i - \mathbf{R}_{\text{std}}(\mathbf{W})_i = \mathbf{0} \quad (i = 0, 1, \dots, N),$$

where  $\mathbf{W}(\mathbf{U}) := \mathbf{W}(\mathbf{U})$  and  $\mathbf{Z}(\xi, t) := \mathcal{Z}(x, t)$  are the entropy variables and their gradients in reference space. The auxiliary variables so calculated are used to compute  $\nabla \mathbf{u}$  and  $\nabla T$ , and subsequently the diffusive flux contribution. The final semi-discrete discretisation for Eq. (14b) can be written as follows.

$$J\dot{\mathbf{U}}_i + (1 - \alpha)\mathbf{R}_{\text{sf}}^{\text{HO}}(\mathbf{F}_a)_i + \alpha\mathbf{R}_{\text{sc}}^{\text{LO}}(\mathbf{F}_a)_i + \mathbf{R}_{\text{std}}(\mathbf{F}_d)_i = \mathbf{0} \quad (i = 0, 1, \dots, N)$$

Here,  $\mathbf{F}_d(\mathbf{U}, \mathbf{Z}) := \mathcal{F}_d(\mathbf{U}, \mathcal{Z})$  is the diffusive flux in reference space, and standard DGSEM discretisation is used for the same. At the element surfaces, entropy variables ( $\mathbf{W}^*$ ) and diffusive flux ( $\mathbf{F}_d^*$ ) are calculated as simple averages of the values across the surface.

### 3.3 Extension to hypersonic regime

In very high speed flows, the presence of a wall boundary layer introduces very high gradients locally, especially in the initial transient. It is found that although the DGSEM-BR1 algorithm described in Section 3.2 works for supersonic flows with explicit RK time integration (see Sections 4.1 to 4.3), it crashes when applied directly to viscous hypersonic flows ( $M_\infty \geq 6$ ). Such simulations are observed to crash immediately, within  $O(1)$  time steps (with CFL  $O(0.1)$ ) when freestream initial condition was used. More specifically, it is observed that as the velocity at the wall starts dropping under the influence of wall boundary condition, the velocity profile develops

a non-monotonic variation and overshoots the freestream value. This produces an undershoot in the temperature profile which steepens until the temperature reaches zero to eventually halt the simulation. For illustration, the velocity and temperature profiles in the first two cells above the wall for a representative simulation are shown in Fig. 2. One can notice the undershoot in temperature developing at  $y = 10.01 \mu\text{m}$ . Similar behaviour was seen if instead the simulation was started with the inviscid solution, or a zero velocity condition.

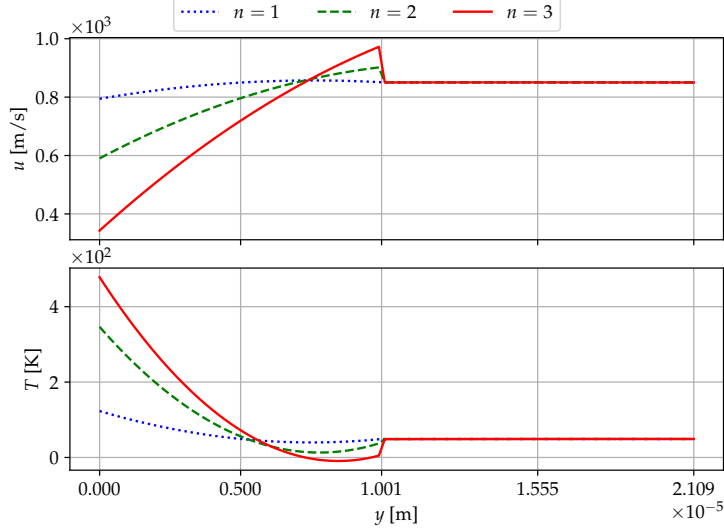


**Figure 2:** Velocity and temperature profiles for a Mach 6 SBLI ( $\text{Re}_L = 1.5 \times 10^5$  case discussed in Section 4.4.2) simulation with unmodified DGSEM-BR1 algorithm ( $N = 2$ ,  $\text{CFL} = 0.1$ ). Time steps are indexed by  $n$ . The grid locations on the horizontal axis match the degree of freedom locations for the first two cells above wall. The simulation crashed in the fourth time step. In the third time step ( $n = 3$ ), although the DG polynomial variation of the temperature has negative values, since it is positive at the DoF locations, the simulation did not crash yet.

The algorithm described Sections 3.1 and 3.2 is from the works of [27, 37], and is found to crash when used directly for hypersonic flows, as described in the previous paragraph. A modification of this algorithm, for extending it to hypersonic regime is now proposed.

Since inviscid hypersonic simulations at the same flow conditions could be simulated without an issue, it is suspected that the calculation of diffusive flux residual is unstable for hypersonic viscous flow simulations. A freestream initial condition is an unphysical flow condition in the context of a viscous flow. In this case, the wall boundary condition specifies a zero interface velocity condition for calculating  $\nabla \mathbf{W}$ :

$$\mathbf{W}^* = \left[ \frac{\gamma - s^*}{\gamma - 1}, 0, 0, 0, 0, -2\beta^* \right]^T.$$

Since the velocity gradient between this interface state and the freestream becomes exceedingly high in hypersonic flows, the diffusive residual contributes significantly to the overall residual in the initial transient. On the other hand, at a wall, the advective boundary flux is calculated using a “ghost” (abbr. “gh”) state having reversed “inner” (abbr. “in”) velocity:

$$\mathbf{U}_{\text{gh}} = \rho_{\text{in}} [1, -u_{\text{in}}, -v_{\text{in}}, -w_{\text{in}}, E_{\text{in}}]^T, \quad \mathcal{F}_{\text{a}}^* = \mathcal{F}_{\text{a}}^*(\mathbf{U}_{\text{gh}}, \mathbf{U}_{\text{in}}, \mathbf{n}_w).$$

For a flat plate case, this sets up a simple shear flow which is preserved by any contact resolving flux scheme (e.g. HLLC). This implies that advective residual would have only a small contribution in this initial phase, making diffusive residual the major contributor. Therefore, to facilitate a stable development of the boundary layer from an unphysical initial condition, the diffusive residual is scaled by introducing  $\alpha_d$  as follows (described again in a one-dimensional setting for simplicity).

$$\alpha_d = \begin{cases} \alpha/\alpha_{\max} & \text{In near wall region,} \\ 0 & \text{Elsewhere.} \end{cases}$$

$$J\dot{\mathbf{U}}_i + (1 - \alpha)\mathbf{R}_{\text{sf}}^{\text{HO}}(\mathbf{F}_{\text{a}})_i + \alpha\mathbf{R}_{\text{sf}}^{\text{LO}}(\mathbf{F}_{\text{a}})_i + (1 - \alpha_d)\mathbf{R}_{\text{std}}(\mathbf{F}_{\text{d}}) = \mathbf{0} \quad (i = 0, 1, \dots, N)$$

For this modification to work however, the value of  $\alpha$  must be sufficiently high in the wall cells during the initial transient (since  $\alpha_d \propto \alpha$ ). Conceivably, shock detectors are designed to identify discontinuities and hence cannot

be expected to detect the high gradients which show-up in the initial transient of hypersonic boundary layers. With the current algorithm (see Section 3.1), while  $\alpha$  does take a non-zero value initially, it diminishes very quickly, much before the boundary layer is reasonably established. For this reason, it becomes necessary that the value of  $\alpha$  at the wall (denoted by  $\alpha_w$ ) is set to stay at a high value initially and then gradually relaxed to the value based on local flow properties (as described in Section 3.1).

$$\alpha'_w = \max\{\alpha_{\text{imposed}}, \alpha_w\}, \quad \alpha_{\text{imposed}} \sim \begin{cases} 0.95\alpha_{\text{max}} & t \leq t_w \\ 0.95\alpha_{\text{max}}(2 - t/t_w) & t_w < t \leq 2t_w \\ 0 & \text{otherwise} \end{cases}$$

It is found that setting  $t_w$  to a few viscous time scales of the first cell, e.g.,  $t_w \sim 5\Delta y_w^2/\nu_\infty$  ( $\Delta y_w$  being the wall cell height), gives reasonable results. This time scale is typically much smaller than any physically relevant time scale. Together, these two modifications ensure that the viscous residual is sufficiently limited in the initial transient. Once this phase passes (i.e.  $t > 2t_w$ ), and the boundary layer development progresses to certain extent, the full contribution of diffusive residual would be restored since  $\alpha = 0 \implies \alpha_d = 0$  at this stage. At the leading edge, however,  $\alpha_d$  remains non-zero throughout the simulation since  $\alpha$  itself is calculated to be non-zero. It was observed that setting  $\alpha_d = 0$  at the leading edge, even in converged solutions, would immediately lead to a crash. A sharp leading edge is again an unphysical feature in viscous simulations and  $\alpha_d$  being non-zero in this region can be considered a numerical resort to simulate it.

In summary, to perform a stable computation of viscous hypersonic flows started from unphysical initial conditions, the viscous residual is scaled near wall up to a few viscous time scales of the first cell. In steady state, this scaling is retained at the leading edge to account for its (unphysical) sharp feature.

### 3.4 Other details and implementation

The formulation of the DGSEM algorithm on curved hexahedral elements in three dimensions can be found in [27, 32, 37]. Boundary conditions are applied in a “weak” sense, by imposing  $\mathbf{W}^*$ ,  $\mathbf{F}_a^*$  and  $\mathbf{F}_d^*$ , according to Mengaldo *et al.* [39]. The resulting semi-discrete equations are advanced in time using explicit Runge-Kutta methods. Although explicit time stepping is less common for hypersonic flow simulations, it has nevertheless been used previously (see for instance [40–45]). In this work, the TVD-RK3 method of Gottlieb & Shu [46] and a 5-stage low storage RK4 method of Kennedy *et al.* [47] are used. The stable time step  $\Delta t_e$  for an element is calculated using Eq. (15a) [11, 48], and the global time step value is subsequently calculated using Eq. (15b),

$$\Delta t_e = \frac{\text{CFL}}{N^{1.5}} \min_{\text{Element nodes}} \left[ \frac{1}{\|\underline{\mathbf{J}}^{-1}\mathbf{u}\|_\infty + \frac{a}{h_e} + \frac{N^2\nu}{h_e^2}} \right], \quad (15a)$$

$$\Delta t = \min_{\text{Elements}} \Delta t_e, \quad (15b)$$

where  $\|\bullet\|_\infty$  denotes the infinite vector norm,  $\underline{\mathbf{J}}$  is the Jacobian matrix for mapping a three-dimensional curved hexahedral element to the reference element, and  $h_e$  is the minimum vertex distance for an element. For steady state problems, convergence can be accelerated by performing local time stepping, in which case, every element uses its own value of  $\Delta t_e$ , for the update [49]. In viscous hypersonic flows, it is sometimes necessary to have grids with a large variation in the cell size. In such cases, to avoid very high disparity in the local time steps, they can be modified as follows [44],

$$\Delta t'_e = \min_{n \in \text{Neighbors}} \{\Delta t_e, \tau_n \Delta t_n, \tau_g \Delta t\},$$

where  $\tau_n$  and  $\tau_g$  are constants that scale the neighbour’s time step and the global time step respectively. Generally  $\tau_n \lesssim 1.1$  and  $\tau_g \sim 10$  yield stable computation. The expression of residual used in monitoring convergence is given in Eq. (16) (following Wang *et al.* [50]).

$$\mathcal{R}^{n+1} := \frac{1}{\|(\rho E)^{n+1}\|_{L^2}} \left\| \frac{(\rho E)^{n+1} - (\rho E)^n}{\Delta t'_e} \right\|_{L^2} \quad (16)$$

The three-dimensional algorithm is implemented in C++ using the deal.II finite element library [51], and is named PLENS. MPI-parallel implementation of the code is written using deal.II’s interfaces to PETSc [52] and p4est [53]. The meshes required for simulations are generated using Gmsh [54] and SALOME [55]. Visualisation and data collection is done using ParaView [56].

## 4 Results and discussion

This section describes the results obtained with the solver PLENS. The test cases described in Sections 4.1 to 4.3 are simulated directly using the DGSEM-BR1 approach described in Section 3.2, without the hypersonic modification (outlined in Section 3.3), and hence serve as a validation of the algorithm's implementation in PLENS. Furthermore, these simulations use entropy variable gradients as auxiliary variables. The hypersonic cases (Sections 4.4 to 4.7) are simulated with the hypersonic modification, and use the conservative variable gradients as auxiliary variables since they are observed to perform better. Unless otherwise mentioned, after an initial transient phase where time accurate simulation is done, all simulations use local time stepping to accelerate convergence to steady state. When local time stepping is used, the simulation time loses physical significance, and, if mentioned, is just a cumulation of the smallest time step value over all the time steps. Unless otherwise mentioned, all simulations use the Chandrashekhar surface flux scheme.

### 4.1 Subsonic boundary layer

A Mach 0.5 boundary layer case described in Mengaldo *et al.* [39] is used as a subsonic viscous test case. The flow conditions are  $\text{Re}_u = 1 \times 10^6 \text{ m}^{-1}$ ,  $M_\infty = 0.5$  and  $T_w = T_\infty = 222 \text{ K}$ .<sup>1</sup> The domain along with the computational mesh used is shown in Fig. 3a. The left and top boundaries are given inflow conditions, while the right boundary is treated as outflow at freestream pressure. The outflow boundary condition incorporates a pressure-based correction for subsonic portion of the flow [39]. The bottom boundary has symmetry and constant temperature wall conditions imposed respectively for  $x < 0$  and  $x \geq 0$ . The mesh has 18 cells in the  $y$ -direction and 42 cells in the  $x$ -direction, with 12 cells along the wall. At the wall, the cell height is chosen to be 1/4th of the boundary layer thickness at  $x = 0.02 \text{ m}$ . Results obtained with 4th degree polynomial basis ( $N = 4$ ), CFL = 0.5 and RK4 time integration are shown in Fig. 3. Figure 3b shows the velocity profile compared, for a qualitative purpose, with the incompressible Blasius solution. Figure 3c compares the skin friction coefficient with a correlation given by Young [57] for compressible laminar boundary layers. In this case, Young's correlation virtually coincides with the incompressible Blasius solution, and the skin friction predicted by simulation matches very well with both of these, sufficiently away from the leading edge ( $x/L \geq 0.1$ ).

### 4.2 Supersonic boundary layer

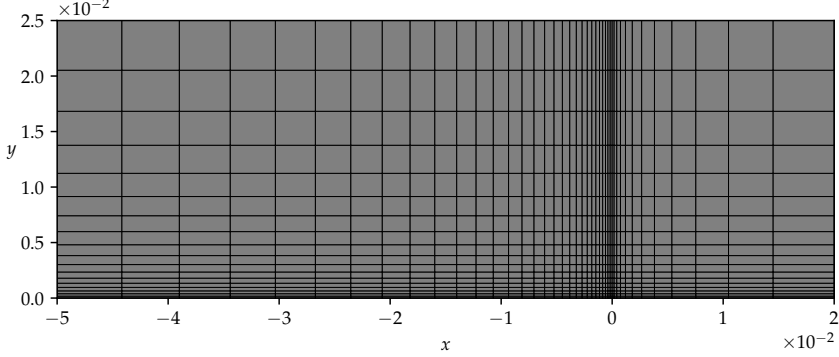
A supersonic BL case proposed by Jacobs [58] is considered here. The flow conditions are  $T_w = T_\infty = 222 \text{ K}$ ,  $M_\infty = 2$  and  $\rho_\infty = 4.04 \times 10^{-3} \text{ kg m}^{-3}$ . The computational domain shown Fig. 4a uses 20 cells in both directions. The minimum cell thickness in the  $y$ -direction is half the BL thickness at  $x = 1 \text{ m}$ . Left and top boundaries are considered inflow and the right boundary is treated as outflow. The bottom boundary is considered a constant temperature wall. Time accurate simulation is performed using CFL = 0.5, with 4th degree polynomial basis ( $N = 4$ ) and RK4 time stepping. Figure 4b compares the results at  $t = 8 \text{ ms}$  with the spectral solution given in [58]. It may be concluded that the agreement with the reference solution is reasonably good.

### 4.3 Mach 2 SBLI

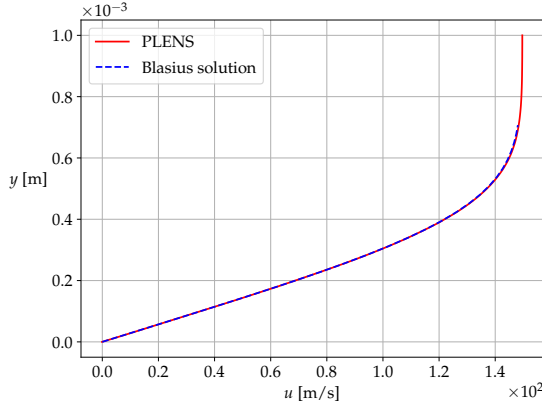
A Mach 2 incident shock-boundary layer interaction experiment by Degrez *et al.* [59] is considered here. The experiment generates a freestream at  $M_\infty = 2.15$  from stagnation conditions  $p_0 = 10.7 \text{ kPa}$  and  $T_0 = 293 \text{ K}$  which is deflected by a wedge of angle  $3.81^\circ$  to generate an oblique shock at an angle  $30.8^\circ$ . These conditions are slightly different from the exact experimental measurements to account for a small misalignment of the plate with the freestream [59, 60]. The oblique shock impinges on an insulated flat plate at a distance  $X_{\text{sh}} = 80 \text{ mm}$  from the leading edge. The computational domain has a height of 40 mm and the shock generation is mimicked using post shock conditions as an inflow boundary condition on one part of the top boundary. The geometry along with the boundary conditions is shown in Fig. 5. The outflow boundary is treated to be at a pressure  $p/p_\infty = 1.539$ , calculated using inviscid shock reflection relations.

A set of 3 meshes for 2nd, 3rd and 4th degree polynomial bases ( $N = 2, 3, 4$ ) is generated such that all of them nominally have the same resolution of  $150 \times 108$  Degrees of Freedom (DoFs). Uniform spacing is used in the  $x$ -direction and the mesh is scaled geometrically in the  $y$ -direction with a progression ratio such that all the three meshes have around 18 DoFs inside the unperturbed boundary layer at  $x = X_{\text{sh}}$ . The exact details are given

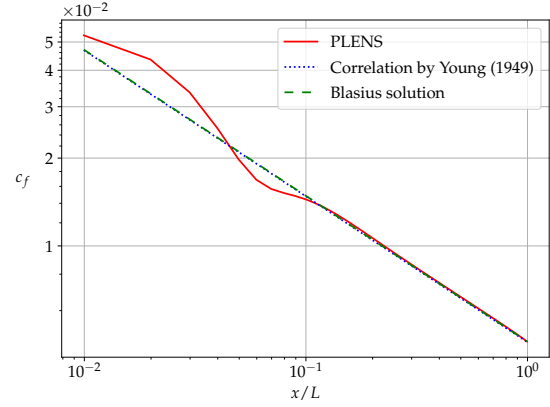
<sup>1</sup> $\text{Re}_u$  denotes the unit Reynolds number  $\rho U/L$ , and  $T_w$  denotes the wall temperature.



(a) Computational grid of size  $42 \times 18$  cells, with 12 cells on the plate. Dimensions are in meters.



(b) Velocity profile comparison.



(c) Skin friction comparison.  $L = 0.02$  m is the plate length.

**Figure 3:** Numerical results of the subsonic boundary layer simulation obtained using 4th degree polynomial basis ( $N = 4$ ),  $CFL = 0.5$  and RK4 time integration method.

in Table 2. All simulations are started using freestream conditions and are run up to an end time of 4 ms (which is about 14 flow time scales) using local time stepping and  $CFL = 0.5$ . TVD-RK3 method is used for  $N = 2$ , while RK4 method is used for  $N = 3$  and 4. For the mentioned end time, all simulations show a drop in residual by 6 orders of magnitude.

Figure 6 compares the predicted pressure variation with the experimental data. All three results match well with the measurements. The discrepancy in the post-reattachment region is within the experimental error limits. Fig. 7 compares the skin friction coefficient with the numerical simulations of Degrez *et al.* [59] and Boin *et al.* [60]. The results obtained here agree closely with those of Boin *et al.* The results of Degrez *et al.* have a different trend since they employ a constant viscosity assumption. Figure 6 also shows that apart from a small difference in the pre-separation region, the pressure profiles predicted by the three simulations are virtually indistinguishable. On the other hand, skin friction profiles shown in Fig. 7 are not similar to such a degree. The value of  $c_f$  before separation is lower for  $N = 2$  compared to  $N = 3, 4$ . The variation of  $c_f$  in the separation region is not very smooth for  $N = 2$ , and this is also reflected in Fig. 6a as a minute perturbation at  $x/X_{sh} \approx 1$ . Finally, Fig. 8 shows the variation of the blending coefficient for the three cases considered.

**Table 2:** Grid specifications for the Mach 2 SBLI simulations. Uniform spacing is used in the  $x$ -direction.

Basis polynomial degree ( $N$ )	Cells	DoFs	Progression ratio in the $y$ -direction
2	$51 \times 36 \times 1$	$153 \times 108 \times 3$	1.104
3	$38 \times 27 \times 1$	$154 \times 108 \times 4$	1.143
4	$30 \times 22 \times 1$	$150 \times 110 \times 5$	1.161

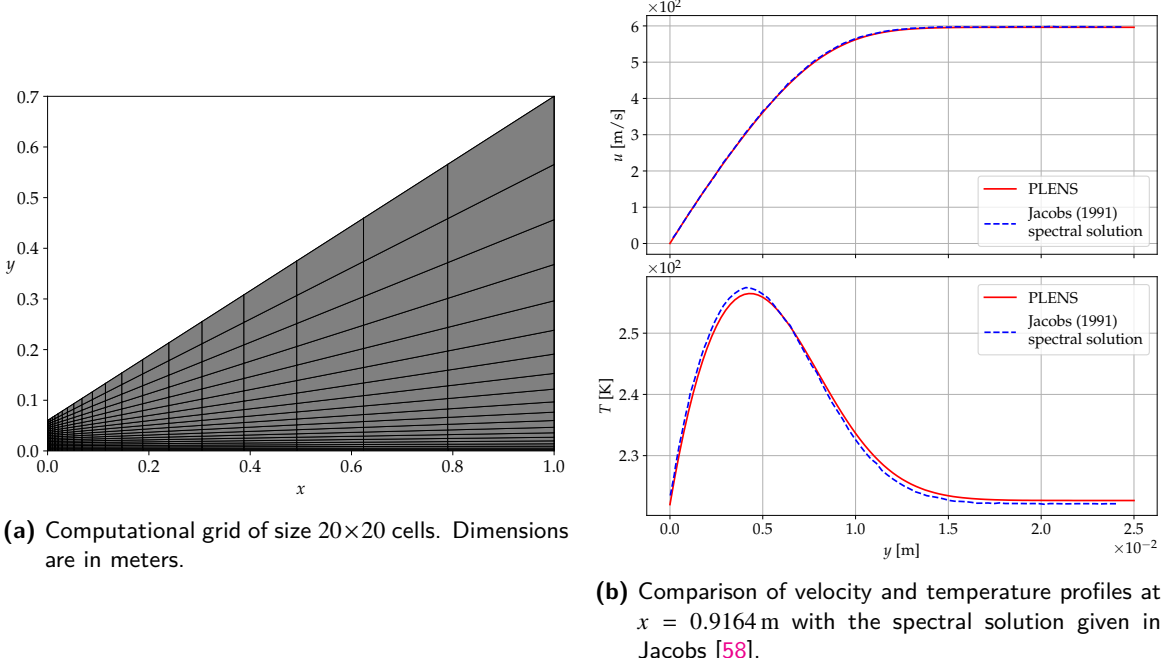


**Figure 4:** Numerical results for the supersonic BL case using 4th degree polynomial basis ( $N = 4$ ), CFL = 0.5 and RK4 time integration.

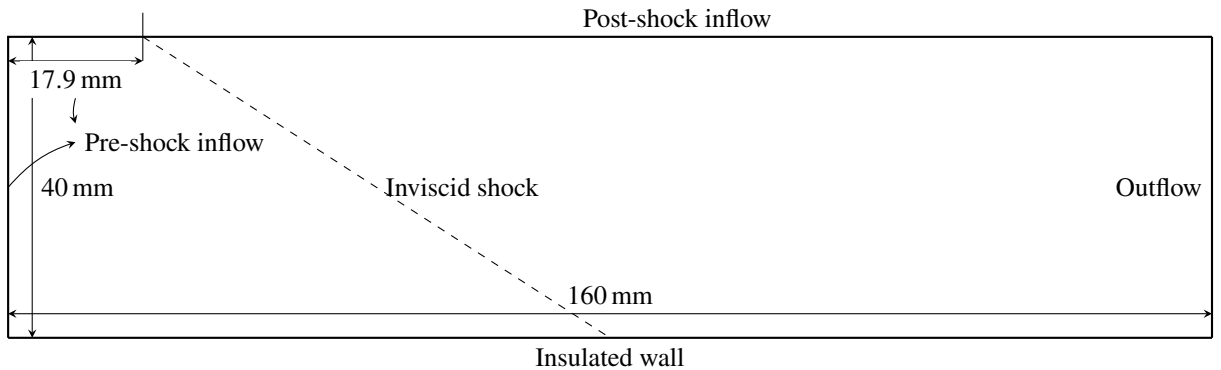


**Figure 5:** Schematic of geometry with boundary conditions for the Mach 2 SBLI case of Degrez *et al.* [59].

#### 4.4 Mach 6 SBLI

A series of laminar SBLI experiments with a hypersonic freestream  $M_\infty = 6.06$  were performed by Lewis *et al.* [61]. The geometry consists of a wedge of angle  $10.25^\circ$  following a flat plate of length  $L = 6.35$  cm. The ramp length is equal to the plate length. Experiments with  $M_\infty = 6.06$  were performed for two different wall conditions: adiabatic and constant temperature at  $T_w/T_{0\infty} = 0.2$ ; and three different freestream Reynolds numbers:  $\text{Re}_L = 1.5 \times 10^5$ ,  $3 \times 10^5$  and  $5 \times 10^5$ . The Reynolds number was varied by keeping the stagnation temperature approximately constant and varying the stagnation pressure.

Unlike the simulations described in Sections 4.1 to 4.3, these simulations require the hypersonic modification proposed in Section 3.3. To recall, in this modification, (i) the viscous residual is scaled by  $(1 - \alpha_d)$  in the near wall region, and (ii) the blender value for the wall cells,  $\alpha_w$ , is modified (as  $\alpha'_w$ ) to have a high value in the initial phase. All simulations use TVD-RK3 time integration and 2nd degree polynomial basis ( $N = 2$ ) unless specified otherwise.

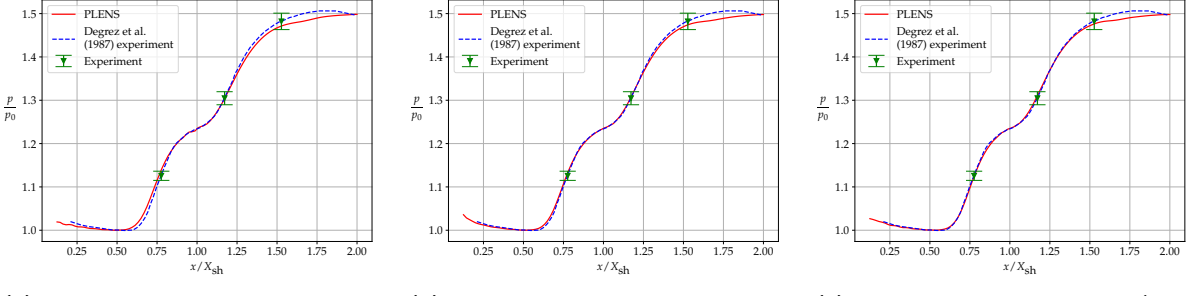


**Figure 6:** Comparison of surface pressure variation with experimental data for the Mach 2 SBLI case of Degrez *et al.* [59]. Here  $p_0$  is the minimum value of pressure over the plate, and is computed from the numerical result.

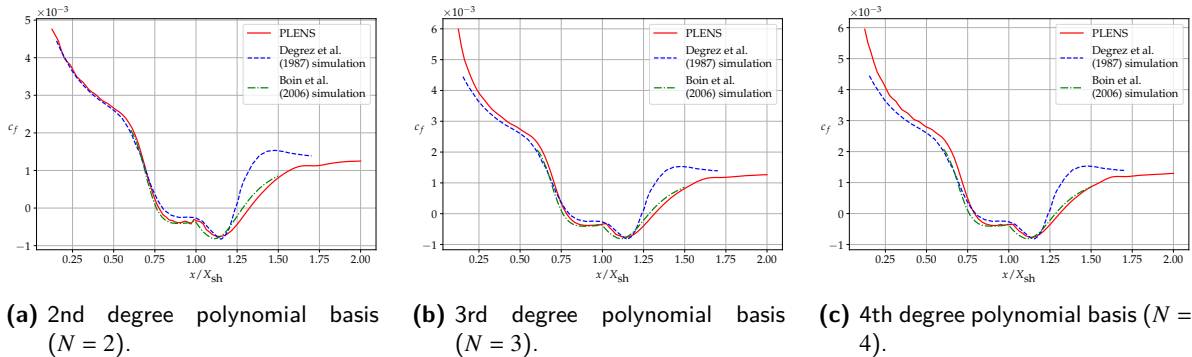


**Figure 7:** Comparison of skin friction variation in Mach 2 SBLI case with numerical results of Degrez *et al.* [59] and Boin *et al.* [60].

#### 4.4.1 Adiabatic wall condition

For the adiabatic wall condition, only the experiment with  $\text{Re}_L = 1.5 \times 10^5$  gave laminar flow throughout the interaction region. Simulations are performed on four different meshes of sizes  $135 \times 60$ ,  $180 \times 80$ ,  $225 \times 80$  and  $180 \times 100$  respectively.<sup>2</sup> The meshes are graded in the wall-normal direction and also in the streamwise direction near the leading edge and corner. While Mesh 1 has  $\Delta y_w = 10 \mu\text{m}$ , Meshes 2 and 3 have  $\Delta y_w = 7.5 \mu\text{m}$ , and Mesh 4 has  $\Delta y_w = 5 \mu\text{m}$ . The resulting cell Reynolds numbers for the first layer of wall cells, based on freestream properties are 24, 18 and 12 respectively. Mesh 1 simulation is performed using  $\text{CFL} = 0.5$  and  $\alpha_{\max} = 0.5$ , with the wall blinder value varied as follows.

$$\alpha'_w = \max\{\alpha_{\text{imposed}}, \alpha_w\}, \quad \alpha_{\text{imposed}} = \begin{cases} 0.475 & t < t_w = 0.4 \mu\text{s} \\ 0.475(2 - t/t_w) & t_w < t < 2t_w \\ 0 & 2t_w < t \end{cases}$$

Elements with center-to-wall distance less than  $500 \mu\text{m}$  are considered ‘‘near wall’’ for scaling the viscous residual (as described in Section 3.3) in all cases. Simulations for Meshes 2 to 4 are initialised with converged solutions on a previous mesh, and hence do not require a modification of  $\alpha_w$ . Figure 9a shows Mesh 1 along with the boundary conditions and Fig. 9b shows the variation of blending coefficient for the simulation using this mesh. Figure 9c shows the pressure variation obtained on all meshes. Clearly, all results are almost identical and agree well with the numerical result of [62], while there is some discrepancy with experiments in the prediction of separation location. In the simulation on Mesh 1, which is started from freestream initial condition, the residual only drops by 3 orders of magnitude and stalls at that level, although there are no visible oscillations in the solution. For Meshes 2 and 3, the residual drops by 1 order of magnitude when initialised with a coarser converged solution, and stalls at that level without any large scale oscillations.<sup>3</sup> For Mesh 4, the residual drops by 3 orders of magnitude when initialised with Mesh 2 converged solution.

<sup>2</sup>Here and in the following text,  $n_1 \times n_2$  indicates that the mesh consists of  $n_1$  and  $n_2$  cells in the streamwise and wall-normal directions respectively.

<sup>3</sup>Mesh 2 and 3 simulations are initialised with converged solutions on Mesh 1 and 2 respectively.

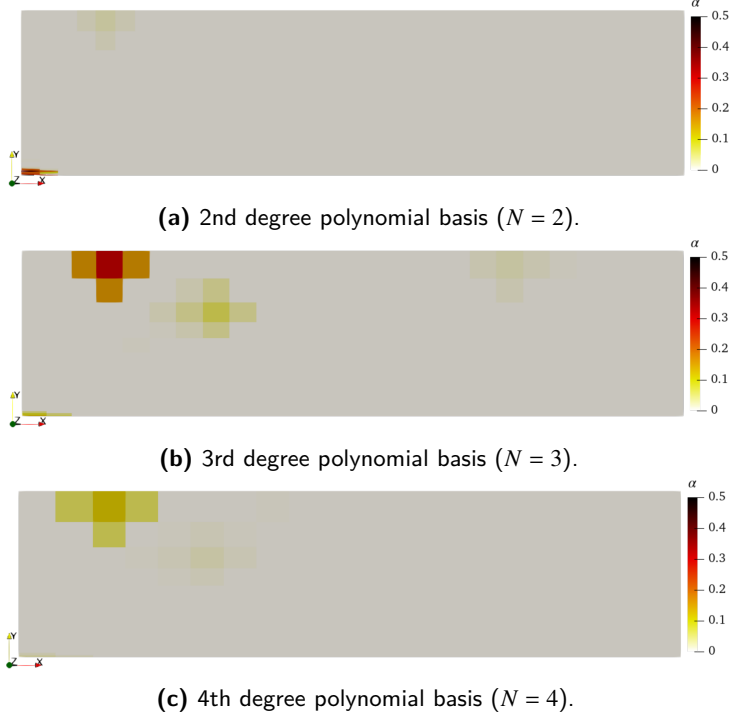


**Figure 8:** Variation of the blender  $\alpha$  in Mach 2 SBLI case.

#### 4.4.2 Constant temperature wall condition

In case of a constant temperature wall (at  $T_w/T_{0\infty} = 0.2$ ), experiments at all three Reynolds numbers displayed laminar flow. Figure 10 shows the results obtained for these three cases. For  $Re_L = 1.5 \times 10^5$  and  $3 \times 10^5$ , two different grids are used to demonstrate the grid convergence. Further, in the case with  $Re_L = 1.5 \times 10^5$ , 3rd and 4th order basis polynomials are also used for simulation with the coarser grid, as shown in Fig. 10a. The residuals drop by 6 and 3 orders of magnitude respectively for  $Re_L = 1.5 \times 10^5$  and  $3 \times 10^5$  on the coarser grids when using  $N = 2$ . In both cases, the finer grid solution (with  $N = 2$ ) is initialised with the converged solution on the coarser grid. Higher order simulations using 3rd and 4th degree polynomial bases ( $N = 3$  and 4) for  $Re_L = 1.5 \times 10^5$  are initialised with converged solution on the same grid with  $N = 2$  and 3 respectively, and use a five-stage RK4 time integrator [47] instead of the TVD-RK3 scheme. For  $Re_L = 5 \times 10^5$ , only one grid is used for simulation and the residual drops 6 orders of magnitude in this case. The numerical results for all values of  $Re_L$  under-predict the separation extent compared to experiment. This observation is also seen in all numerical results (including Carter's result [62]) for the adiabatic wall case presented in Section 4.4.1. This consistent discrepancy might be due to uncertainties in experimental arrangement and/or measurement.

## 4.5 Mach 11 SBLI

A blind validation study was performed by Harvey *et al.* [63] in the year 2001 to assess the CFD capabilities of laminar hypersonic codes. The experiments for this validation study were performed by Holden & Wadhams [64] on cylinder/flare and cone/cone (or double cone) configurations at laminar perfect gas conditions. For a blind validation, these experimental results were not made available until numerical results were submitted.

The hollow cylinder/extended flare (HCEF) model's Run 9 is considered here for simulation. The geometry for the HCEF model consists of a cylinder followed by a  $30^\circ$  flare, as shown in Fig. 11. The freestream conditions for Run 9 are  $u_\infty = 2566 \text{ m s}^{-1}$ ,  $T_\infty = 121.1 \text{ K}$  and  $\rho_\infty = 0.845 \times 10^{-3} \text{ kg m}^{-3}$ , giving  $M_\infty = 11.44$  and  $Re_u = 264\,830 \text{ m}^{-1}$  [65]. The wall is treated as a constant temperature surface at  $T_w = 296.7 \text{ K}$ .

Simulation is performed on a mesh of size  $136 \times 45$  cells using 2nd degree polynomial basis ( $N = 2$ ),  $CFL = 0.3$  and TVD-RK3 time integration. At the wall, a cell size of  $\Delta y_w = 50 \mu\text{m}$  is used which gives a freestream based cell Reynolds number of 13. The resulting mesh is shown in Fig. 12a. Here,  $\alpha_{\max} = 1$  is used along with the

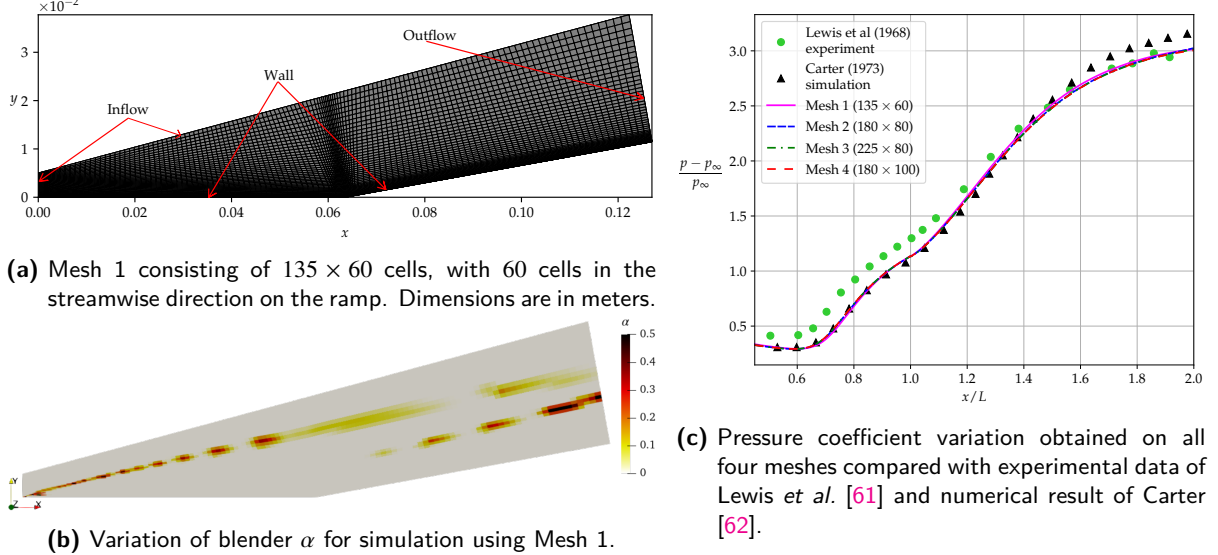


**Figure 9:** Numerical results obtained for the Mach 6 SBLI case: adiabatic wall at  $Re_L = 1.5 \times 10^5$ .

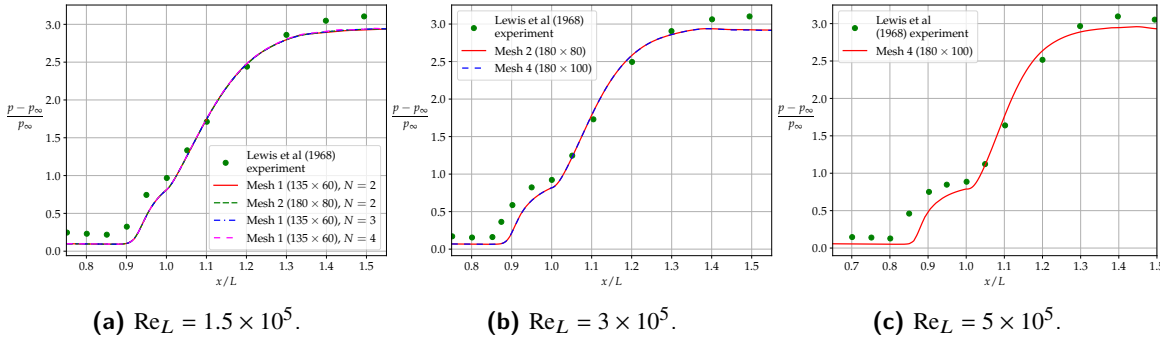


**Figure 10:** Surface pressure variation obtained for Mach 6 SBLI case: constant temperature wall at three freestream Reynolds numbers.

following variation for  $\alpha$  at the wall.

$$\alpha'_w = \max\{\alpha_{\text{imposed}}, \alpha_w\}, \quad \alpha_{\text{imposed}} = \begin{cases} 0.99 & t < t_w = 0.7 \mu\text{s} \\ 0.99(2 - t/t_w) & t_w < t < 2t_w \\ 0 & 2t_w < t \end{cases}$$

Elements with center-to-wall distance less than  $600 \mu\text{m}$  are considered “near wall”. Figure 12 shows the results obtained for this case using two different surface flux schemes: Chandrashekhar and Rusanov-HLLC. The residual dropped by 3 orders of magnitude for both the simulations. Figs. 12d and 12e show that while the two flux schemes give almost identical results, the separation extent is over-predicted, leading to slight discrepancies in separation and reattachment locations. While reattachment peak values are lower, surface pressure and heat transfer results follow the trend of Gnoffo’s numerical result [65]. A slight over-prediction in heat transfer on the cylinder surface is visible in Fig. 12e, both before and inside the separation region. This, along with the under-prediction of the peak value, is possibly due to insufficient grid resolution near the wall.

To improve the results, simulation using a refined mesh is attempted. These finer grid simulations (using both flux schemes), however, produce large scale oscillations in the separation bubble which eventually lead to complete distortion of the flow features. While improvement in surface pressure and heat transfer results is observed initially, eventually, oscillations start developing due to expansion and re-compression of reverse flow on the cylinder. Figure 13 illustrates this flow behaviour on a fine grid of size  $180 \times 64$  with  $\Delta y_w = 30 \mu\text{m}$ . This distortion in the reverse flow subsequently induces large scale oscillations which disrupt the entire outer shock structure. Various measures taken to mitigate this issue, like reducing the CFL number, increasing RK time integration order, and using a more dissipative surface flux scheme such as Rusanov prove to be ineffective. Difficulties in obtaining converged solution with an explicit time integration was also reported previously in the context of FVM (for instance, see Candler *et al.* [67] and Reimann & Hannemann [43]) for such class of flows. Therefore, for hypersonic flows

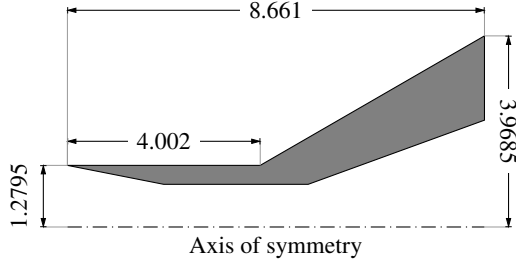


**Figure 11:** Hollow cylinder extended flare (HCEF) model [66]. Computational domain is on the outer side of this axisymmetric geometry. Dimensions are in inches.

with very high Mach numbers ( $M_\infty \gtrsim 10$ ), explicit time integration with local time stepping may not be a suitable choice for steady state calculations with the current DGSEM algorithm being used. The possibility of obtaining a converged solution using time-accurate simulation is not explored due to the impractical wall clock time it requires.

The same issue is also observed with the other HCEF experimental runs: Run 8, Run 11 and Run 14. In all these cases, while a coarser grid gives a converged solution (albeit with discrepancies in separation extent), a finer grid simulation displays such large scale oscillations and diverges.

## 4.6 Mach 14 SBLI

Experiments for Mach 14 laminar flow over wedge geometries were performed by Holden & Moselle [68]. For the case considered here, air at freestream conditions  $p_\infty = 9.995 \text{ Pa}$ ,  $T_\infty = 72.22 \text{ K}$  and  $M_\infty = 14.1$  flows over a plate of length  $L = 0.4389 \text{ m}$  followed by a  $24^\circ$  ramp of the same length in  $x$  direction. Both the plate and the ramp are treated as constant temperature surfaces at  $T_w = 297.2 \text{ K}$ . Two meshes are considered for the two-dimensional simulations here: Mesh 1 of size  $131 \times 44$  with  $\Delta y_w = 300 \mu\text{m}$  and Mesh 2 of size  $195 \times 66$  with  $\Delta y_w = 207 \mu\text{m}$ . The results obtained on Mesh 1 with  $\text{CFL} = 0.3$ , 2nd degree polynomial basis ( $N = 2$ ) and TVD-RK3 time integration are shown in Fig. 14. The wall blinder value is varied as follows in this case.

$$\alpha'_w = \max\{\alpha_{\text{imposed}}, \alpha_w\}, \quad \alpha_{\text{imposed}} = \begin{cases} 0.99 & t < t_w = 0.6 \mu\text{s} \\ 0.99(2 - t/t_w) & t_w < t < 2t_w \\ 0 & 2t_w < t \end{cases}$$

Elements with center-to-wall distance less than 1.5 mm are considered ‘near wall’. The two-dimensional simulation result obtained here over-predicts separation extent in this case, as is also observed in the numerical result of Rudy *et al.* [69] which uses an FVM on  $201 \times 201$  two-dimensional grid. Similar to the observations of simulations presented in Section 4.5, the finer simulation on Mesh 2 displays large scale oscillations in separation bubble which eventually lead to divergence of the simulation.

## 4.7 Mach 8 flow over cylinder

All the hypersonic cases considered so far were SBLI configurations. In this section, a hypersonic Mach 8 flow over a cylinder, described in Kitamura *et al.* [70], is considered for simulation. Air at freestream conditions  $M_\infty = 8.1$ ,  $p_\infty = 370.7 \text{ Pa}$  and  $T_\infty = 73.73 \text{ K}$  flows over a cylinder of radius  $r_0 = 20 \text{ mm}$  which is maintained at a constant temperature  $T_w = 300 \text{ K}$ . Three different simulations are performed for this case. In the first two simulations, the cylindrical computational domain  $(r, \phi) \in [r_0, 2.5r_0] \times [-\phi_0, \phi_0]$  (with  $\phi_0 = 75^\circ$ ) is meshed with 100 cells in radial and azimuthal directions. The mesh is graded with a geometrical progression in the radial direction to get a wall cell size  $\Delta r_w = 0.4 \mu\text{m}$ , thus giving a freestream-based cell Reynolds number of 2.6. Further, these simulations use 2nd degree polynomial basis ( $N = 2$ ),  $\text{CFL} = 0.3$ , TVD-RK3 time stepping and  $\alpha_{\text{max}} = 1$ , along with the following variation of wall blinder value.

$$\alpha'_w = \max\{\alpha_{\text{imposed}}, \alpha_w\}, \quad \alpha_{\text{imposed}} = \begin{cases} 0.99 & t < t_w = 1 \text{ ps} \\ 0.99(2 - t/t_w) & t_w < t < 2t_w \\ 0 & 2t_w < t \end{cases}$$

In the third simulation, the domain is meshed using 150 cells in both directions and 1st degree polynomial basis ( $N = 1$ ) is used. The wall cell size in this case is  $\Delta r_w = 0.2 \mu\text{m}$ . The other parameters are kept unchanged. In all

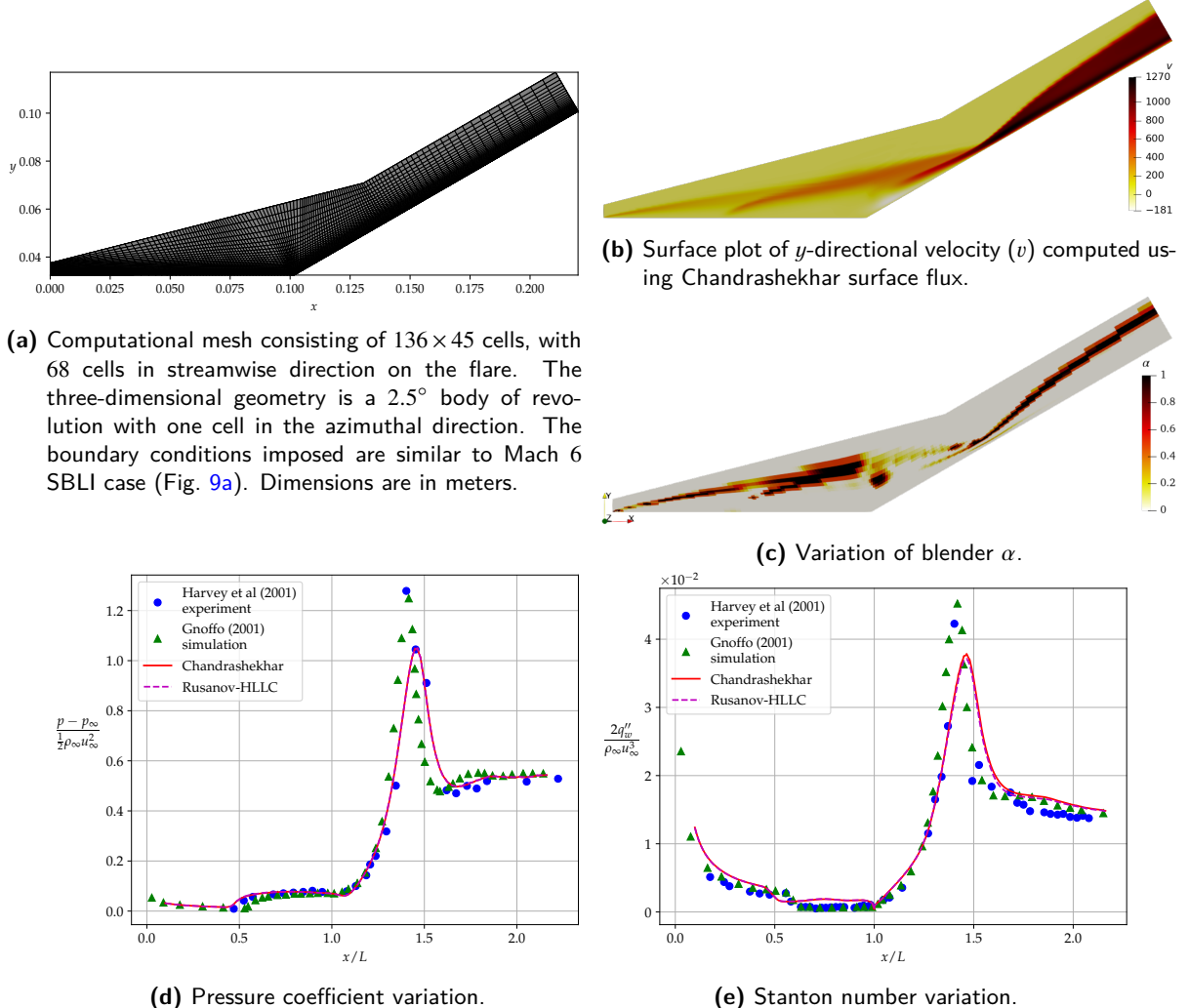


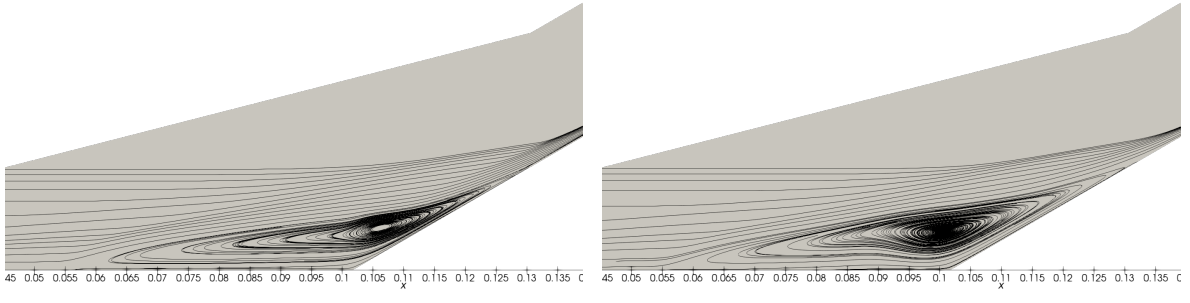
**Figure 12:** Numerical results for Mach 11 SBLI case (HCEF Run 9) on a coarse grid using  $136 \times 45$  cells, 2nd degree polynomial basis ( $N = 2$ ) and CFL = 0.3. Figs. (d) and (e) compare the numerical predictions with experimental data of Harvey *et al.* [63] and the numerical result of Gnoffo [65]. The results obtained using Chandrashekhar and Rusanov-HLLC fluxes are nearly indistinguishable in Figs. (d) and (e).

cases, elements with center-to-wall distance less than  $30\text{ }\mu\text{m}$  are considered ‘near wall’. The different meshes used in these three simulations are designed to have same the DoF count in the  $r\text{-}\phi$  plane, taking into account that they use different values of  $N$ . These settings are summarised in Table 3.

**Table 3:** Settings for different simulations considered for the Mach 8 flow over a cylinder.

Simulation #	Mesh size	$\Delta r_w$	Basis polynomial degree ( $N$ )	Surface flux scheme
1	$100 \times 100$	$0.4\text{ }\mu\text{m}$	2	Chandrashekhar
2	$100 \times 100$	$0.4\text{ }\mu\text{m}$	2	Rusanov-HLLC
3	$150 \times 150$	$0.2\text{ }\mu\text{m}$	1	Chandrashekhar

Figure 15 shows the results obtained for the simulations performed in this case. Due to the very high cell aspect ratio near the wall, the local time step was limited to 10 times the global value initially, until the shock stand-off distance increases to a sufficient value. Subsequently, this limit was removed. For simulations using  $N = 2$ , the steady state residual drops by three orders of magnitude and stagnates at that value thereafter. For the simulation using  $N = 1$ , this residual drops only by one order of magnitude. As shown in Fig. 15a, the surface pressure distribution of Simulation #1 agrees well with the FV numerical result of Kitamura *et al.* [70] on  $160 \times 160$  cells using  $\Delta r_w = 0.2\text{ }\mu\text{m}$ . This is observed for all the simulations considered (not shown in Fig. 15a). The heat transfer prediction of the first two simulations that use  $N = 2$  display some oscillations in the stagnation region,



(a) Converged solution on coarser grid (used as initial condition).

(b) Intermediate solution on finer grid.

**Figure 13:** Streamline pattern observed in a finer grid simulation of Mach 11 SBLI case (HCEF Run 9). The development of a secondary separation region may be noticed in Fig. (b). Dimensions are in meters.

as shown in Figs. 15b and 15e. While the third simulation using  $N = 1$  does not show oscillations, it displays an overshoot in the stagnation heat flux. This highlights that the stagnation region heat flux prediction can depend significantly on the  $N$ , even if the DoF count is kept constant. It seems possible that the oscillations in surface heat transfer in the simulations using  $N = 2$  are due to small-scale unsteadiness in the stagnation region, which, being a low velocity region, may behave like the separation bubble of SBLI simulations.

## 5 Conclusion

An extension of a subcell limiter algorithm has been proposed for high order DG simulations of laminar perfect gas hypersonic flows. The proposed extension builds on the BR1 scheme for the compressible NS equations, and is based on scaling the viscous residual near walls for a stable computation of the high gradients featuring in the initial transient of hypersonic boundary layers. The extension to hypersonic regime has been validated using various hypersonic SBLI test cases. At a low-hypersonic freestream Mach number of  $M_\infty \approx 6$ , stable and accurate grid-converged high order solutions using a quadratic basis have been obtained. At higher Mach numbers ( $M_\infty \gtrsim 10$ ), high order solutions using quadratic basis have been obtained on coarser grids. Importantly, it has been shown that the surface pressure and heat transfer predictions have nearly identical profiles for the two different flux schemes considered in this study. This finding is consistent with the results presented by Ching *et al.* [26] to highlight that high order solutions of hypersonic SBLI flows may alleviate the sensitivity of heat transfer predictions.

At higher mesh resolutions, however, it has been observed that the SBLI simulations at very high hypersonic Mach numbers exhibit large scale oscillations in the separation bubble, eventually leading to divergence of the steady-state solution. Given that convergence issues in hypersonic SBLI simulations using explicit time integration schemes have also been previously reported in FV simulations, it is plausible that the use of local time stepping with explicit time integration is causing the steady-state divergence. Hypersonic flows exhibit a large variation in flow properties as one moves from the wall to the freestream. Additionally, these flow simulations also generally require highly stretched meshes for accurate prediction of wall surface quantities. Together, these two aspects lead to a very rapid variation in the element-local stable time step. For instance, in the coarse grid simulation of the Mach 11 SBLI (Section 4.5), the ratio of stable local time step at the leading edge to that in the freestream region is of the order  $1 \times 10^{-3}$ . This is in stark contrast to the Mach 2 SBLI simulation (Section 4.3) where this ratio was of the order  $1 \times 10^{-1}$ . Results obtained in the current work suggest that explicit time integration with local stepping may not always be suitable for such class of flows in which the local time step has such high variation. Furthermore, it is impractical to perform time accurate simulations of such flows with an explicit method (which must obey a stringent  $CFL \leq 1$  condition) because the separation bubble may require about hundred flow time scales to converge [71]. Therefore, for the steady-state simulation of hypersonic SBLI flows, it may be more appropriate to use semi-implicit or fully implicit time stepping methods that can afford a significantly higher CFL number. Accordingly, developing a robust DG algorithm that uses an implicit time integration scheme along with the subcell limiter of Hennemann *et al.* [27] for hypersonic flows can be a sequel of consequence to this work. Finally, development of a robust detector which can identify both shocks and regions of high gradients that develop in the transient behaviour of wall boundary layers would also be a useful contribution in the context of this work.

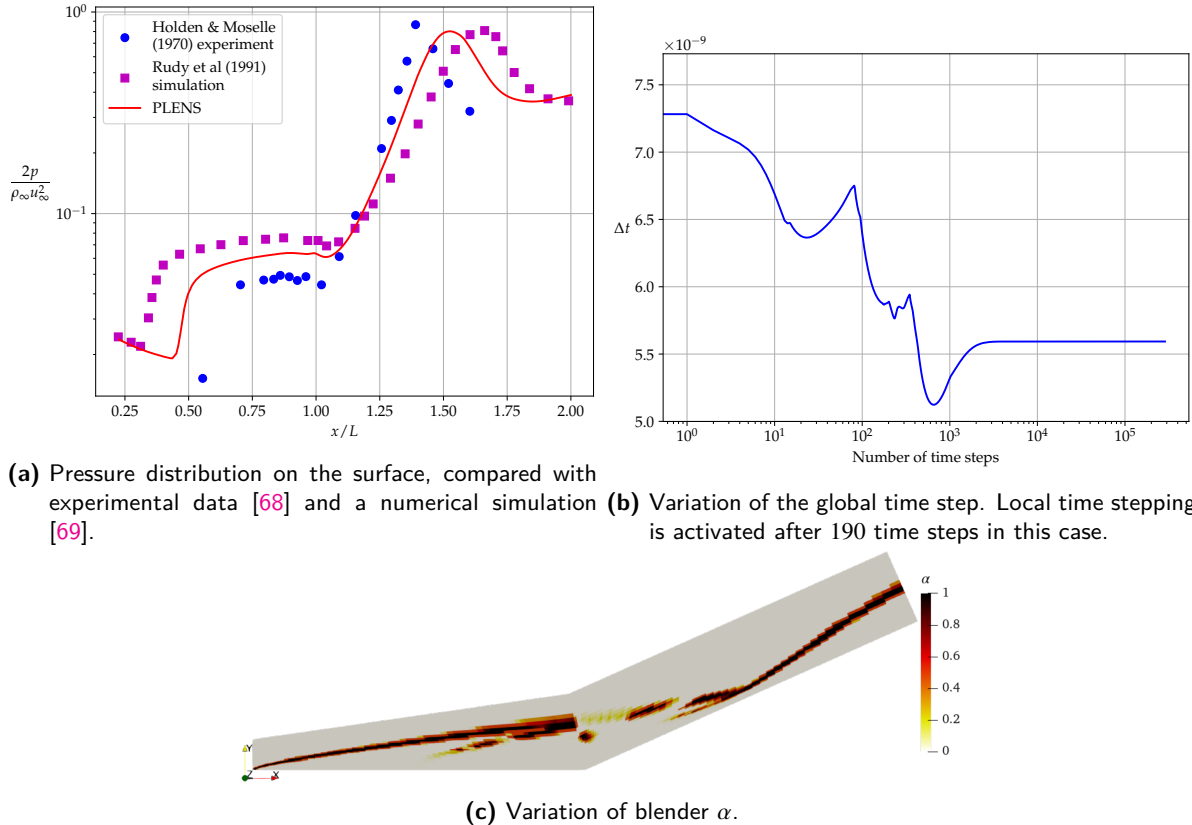


**Figure 14:** Results obtained for Mach 14 SBLI simulation on Mesh 1.

## References

1. Knight, D., Longo, J., Drikakis, D., Gaitonde, D., Lani, A., Nompelis, I., Reimann, B. & Walpot, L. Assessment of CFD capability for prediction of hypersonic shock interactions. *Progress in Aerospace Sciences* **48-49**, 8–26. doi: <https://doi.org/10.1016/j.paerosci.2011.10.001> (2012).
2. Knight, D., Chazot, O., Austin, J., Badr, M. A., Candler, G., Celik, B., de Rosa, D., Donelli, R., Komives, J., Lani, A., Levin, D., Nompelis, I., Panesi, M., Pezzella, G., Reimann, B., Tumuklu, O. & Yuceil, K. Assessment of predictive capabilities for aerodynamic heating in hypersonic flow. *Progress in Aerospace Sciences* **90**, 39–53. doi: <https://doi.org/10.1016/j.paerosci.2017.02.001> (2017).
3. Candler, G., Mavriplis, D. & Trevino, L. *Current status and future prospects for the numerical simulation of hypersonic flows* in *47th AIAA Aerospace Sciences Meeting Including the New Horizons Forum and Aerospace Exposition* (2009), 153. doi: <https://doi.org/10.2514/6.2009-153>.
4. Gaitonde, D. V. Progress in Shock Wave/Boundary Layer Interactions. *Progress in Aerospace Sciences* **72**, 80–99. doi: <https://doi.org/10.1016/j.paerosci.2014.09.002> (2015).
5. Greenshields, C. J., Weller, H. G., Gasparini, L. & Reese, J. M. Implementation of semi-discrete, non-staggered central schemes in a colocated, polyhedral, finite volume framework, for high-speed viscous flows. *International Journal for Numerical Methods in Fluids* **63**, 1–21. doi: <https://doi.org/10.1002/fld.2069> (2010).
6. Frauholz, S., Behr, M., Reinartz, B. & Müller, S. *Numerical simulation of hypersonic air intake flow in scramjet propulsion using a mesh-adaptive approach* in *18th AIAA/3AF International Space Planes and Hypersonic Systems and Technologies Conference* (2012), 5976. doi: <https://doi.org/10.2514/6.2012-5976>.
7. Schwing, A., Nompelis, I. & Candler, G. V. *Parallelization of unsteady adaptive mesh refinement for unstructured Navier-Stokes solvers* in *7th AIAA Theoretical Fluid Mechanics Conference* (2014), 3080. doi: <https://doi.org/10.2514/6.2014-3080>.
8. Mawlood, M. K., Basri, S., Asrar, W., Omar, A. A., Mokhtar, A. S. & Ahmad, M. Solution of Navier-Stokes equations by fourth-order compact schemes and AUSM flux splitting. *International Journal of Numerical Methods for Heat and Fluid Flow* **16**, 107–120. doi: <https://doi.org/10.1108/09615530610636982> (2006).
9. Shen, Y., Zha, G. & Huerta, M. *Simulation of Hypersonic Shock Wave/Boundary Layer Interaction Using High Order WENO Scheme* in *48th AIAA Aerospace Sciences Meeting Including the New Horizons Forum and Aerospace Exposition* (2010). doi: <https://doi.org/10.2514/6.2010-1047>.

10. Cockburn, B. & Shu, C.-W. Runge-Kutta Discontinuous Galerkin methods for convection-dominated problems. *Journal of Scientific Computing* **16**, 173–261. doi: <https://doi.org/10.1023/A:1012873910884> (2001).
11. Hesthaven, J. S. & Warburton, T. *Nodal discontinuous Galerkin methods: algorithms, analysis, and applications* doi: <https://doi.org/10.1007/978-0-387-72067-8> (Springer Science & Business Media, 2007).
12. Cockburn, B., Karniadakis, G. E. & Shu, C.-W. in *Discontinuous Galerkin methods: theory, computation and applications* (eds Cockburn, B., Karniadakis, G. E. & Shu, C.-W.) chap. 1 (Springer Science & Business Media, 2012). doi: <https://doi.org/10.1007/978-3-642-59721-3>.
13. Carpenter, M. H., Parsani, M., Nielsen, E. J. & Fisher, T. C. Towards an Entropy Stable Spectral Element Framework for Computational Fluid Dynamics in 54th AIAA Aerospace Sciences Meeting (2016). doi: <https://doi.org/10.2514/6.2016-1058>.
14. Parsani, M., Boukharfane, R., Nolasco, I. R., Del Rey Fernández, D. C., Zampini, S., Hadri, B. & Dalcin, L. High-order accurate entropy-stable discontinuous collocated Galerkin methods with the summation-by-parts property for compressible CFD frameworks: Scalable SSDC algorithms and flow solver. *Journal of Computational Physics* **424**, 109844. doi: <https://doi.org/10.1016/j.jcp.2020.109844> (2021).
15. Parsani, M., Carpenter, M. H. & Nielsen, E. J. Entropy stable wall boundary conditions for the three-dimensional compressible Navier–Stokes equations. *Journal of Computational Physics* **292**, 88–113. doi: <https://doi.org/10.1016/j.jcp.2015.03.026> (2015).
16. Dalcin, L., Rojas, D., Zampini, S., Del Rey Fernández, D. C., Carpenter, M. H. & Parsani, M. Conservative and entropy stable solid wall boundary conditions for the compressible Navier–Stokes equations: Adiabatic wall and heat entropy transfer. *Journal of Computational Physics* **397**, 108775. doi: <https://doi.org/10.1016/j.jcp.2019.06.051> (2019).
17. Kirk, B. S. & Carey, G. F. Validation Studies of Fully Implicit, Parallel Finite Element Simulations of Laminar Hypersonic Flows. *AIAA Journal* **48**, 1025–1036. doi: <https://doi.org/10.2514/1.40860> (2010).
18. Kirk, B. S., Stogner, R. H., Bauman, P. T. & Oliver, T. A. Modeling hypersonic entry with the fully-implicit Navier–Stokes (FIN-S) stabilized finite element flow solver. *Computers & Fluids* **92**, 281–292. doi: <https://doi.org/10.1016/j.compfluid.2013.10.003> (2014).
19. Holst, K. R., Glasby, R. S., Erwin, J. T., Stefanski, D. L., Bond, R. B. & Schmisser, J. D. *High-Order Simulations of Shock Problems using HPCM CREATE (TM)-AV Kestrel COFFE* in 2018 AIAA Aerospace Sciences Meeting (2018), 1301. doi: <https://doi.org/10.2514/6.2018-1301>.
20. Seguin, J., Gao, S., Habashi, W. G., Isola, D. & Baruzzi, G. A finite element solver for hypersonic flows in thermochemical non-equilibrium, Part I. *International Journal of Numerical Methods for Heat & Fluid Flow*. doi: <https://doi.org/10.1108/HFF-09-2018-0498> (2019).
21. Gao, S., Seguin, J., Habashi, W. G., Isola, D. & Baruzzi, G. A finite element solver for hypersonic flows in thermochemical non-equilibrium, Part II. *International Journal of Numerical Methods for Heat & Fluid Flow*. doi: <https://doi.org/10.1108/HFF-12-2018-0725> (2019).
22. Bhatia, A., Roy, S. & Gosse, R. *2-D hypersonic non-equilibrium flow simulation using rp adaptive time-implicit discontinuous Galerkin method* in 51st AIAA Aerospace Sciences Meeting including the New Horizons Forum and Aerospace Exposition (2013), 302. doi: <https://doi.org/10.2514/6.2013-302>.
23. Barter, G. E. & Darmofal, D. L. Shock capturing with PDE-based artificial viscosity for DGFEM: Part I. Formulation. *Journal of Computational Physics* **229**, 1810–1827. doi: <https://doi.org/10.1016/j.jcp.2009.11.010> (2010).
24. Burgess, N. & Mavriplis, D. *Computing Shocked Flows with High-order Accurate Discontinuous Galerkin Methods* in 42nd AIAA Fluid Dynamics Conference and Exhibit (2012). doi: <https://doi.org/10.2514/6.2012-2715>.
25. Brazell, M. J. & Mavriplis, D. J. *3D mixed element discontinuous Galerkin with shock capturing* in 21st AIAA Computational Fluid Dynamics Conference (2013), 3064. doi: <https://doi.org/10.2514/6.2013-3064>.
26. Ching, E. J., Lv, Y., Gnoffo, P., Barnhardt, M. & Ihme, M. Shock capturing for discontinuous Galerkin methods with application to predicting heat transfer in hypersonic flows. *Journal of Computational Physics* **376**, 54–75. doi: <https://doi.org/10.1016/j.jcp.2018.09.016> (2019).
27. Hennemann, S., Rueda-Ramírez, A. M., Hindenlang, F. J. & Gassner, G. J. A provably entropy stable subcell shock capturing approach for high order split form DG for the compressible Euler equations. *Journal of Computational Physics* **426**, 109935. doi: <https://doi.org/10.1016/j.jcp.2020.109935> (2021).
28. White, F. M. & Corfield, I. *Viscous fluid flow* (McGraw-Hill New York, 2006).
29. Fisher, T. C., Carpenter, M. H., Nordström, J., Yamaleev, N. K. & Swanson, C. Discretely conservative finite-difference formulations for nonlinear conservation laws in split form: Theory and boundary conditions. *Journal of Computational Physics* **234**, 353–375. doi: <https://doi.org/10.1016/j.jcp.2012.09.026> (2013).
30. Carpenter, M. H., Fisher, T. C., Nielsen, E. J. & Frankel, S. H. Entropy Stable Spectral Collocation Schemes for the Navier–Stokes Equations: Discontinuous Interfaces. *SIAM Journal on Scientific Computing* **36**, B835–B867. doi: <https://doi.org/10.1137/130932193> (2014).

31. Fisher, T. C. & Carpenter, M. H. High-order entropy stable finite difference schemes for nonlinear conservation laws: Finite domains. *Journal of Computational Physics* **252**, 518–557. doi: <https://doi.org/10.1016/j.jcp.2013.06.014> (2013).
32. Gassner, G. J., Winters, A. R. & Kopriva, D. A. Split form nodal discontinuous Galerkin schemes with summation-by-parts property for the compressible Euler equations. *Journal of Computational Physics* **327**, 39–66. doi: <https://doi.org/10.1016/j.jcp.2016.09.013> (2016).
33. Chandrashekar, P. Kinetic energy preserving and entropy stable finite volume schemes for compressible Euler and Navier–Stokes equations. *Communications in Computational Physics* **14**, 1252–1286. doi: <https://doi.org/10.4208/cicp.170712.010313a> (2013).
34. Persson, P.-O. & Peraire, J. *Sub-cell shock capturing for discontinuous Galerkin methods* in *44th AIAA Aerospace Sciences Meeting and Exhibit* (2006), 112. doi: <https://doi.org/10.2514/6.2006-112>.
35. Ismail, F. & Roe, P. L. Affordable, entropy-consistent Euler flux functions II: Entropy production at shocks. *Journal of Computational Physics* **228**, 5410–5436. doi: <https://doi.org/10.1016/j.jcp.2009.04.021> (2009).
36. Bassi, F. & Rebay, S. A High-Order Accurate Discontinuous Finite Element Method for the Numerical Solution of the Compressible Navier–Stokes Equations. *Journal of Computational Physics* **131**, 267–279. doi: <https://doi.org/10.1006/jcph.1996.5572> (1997).
37. Gassner, G. J., Winters, A. R., Hindenlang, F. J. & Kopriva, D. A. The BR1 scheme is stable for the compressible Navier–Stokes equations. *Journal of Scientific Computing* **77**, 154–200. doi: <https://doi.org/10.1016/j.jcp.2018.02.020> (2018).
38. Harten, A. On the symmetric form of systems of conservation laws with entropy. *Journal of Computational Physics* **49**, 151–164. doi: [https://doi.org/10.1016/0021-9991\(83\)90118-3](https://doi.org/10.1016/0021-9991(83)90118-3) (1983).
39. Mengaldo, G., Grazia, D. D., Witherden, F., Farrington, A., Vincent, P., Sherwin, S. & Peiro, J. *A Guide to the Implementation of Boundary Conditions in Compact High-Order Methods for Compressible Aerodynamics* in *7th AIAA Theoretical Fluid Mechanics Conference* (2014). doi: <https://doi.org/10.2514/6.2014-2923>.
40. Van Keuk, J., Ballmann, J., Schneider, A. & Koschel, W. *Numerical simulation of hypersonic inlet flows* in *8th AIAA International Space Planes and Hypersonic Systems and Technologies Conference* (1998), 1526. doi: <https://doi.org/10.2514/6.1998-1526>.
41. Moradi, H. V. & Hosseinalipour, M. *On the Performance of AUSM Based Schemes in Hypersonic Flow with Equilibrium Gas Effects* in *14th AIAA/AHI Space Planes and Hypersonic Systems and Technologies Conference* (2006), 7962. doi: <https://doi.org/10.2514/6.2006-7962>.
42. Mack, A. & Hannemann, V. *Validation of the unstructured DLR-TAU-Code for Hypersonic Flows* in *32nd AIAA Fluid dynamics conference and exhibit* (2002), 3111. doi: <https://doi.org/10.2514/6.2002-3111>.
43. Reimann, B. & Hannemann, V. *Numerical investigation of double-cone and cylinder experiments in high enthalpy flows using the DLR TAU code* in *48th AIAA Aerospace Sciences Meeting Including the New Horizons Forum and Aerospace Exposition* (2010), 1282. doi: <https://doi.org/10.2514/6.2010-1282>.
44. Damm, K. A., Landsberg, W. O., Mecklem, S. & Veeraragavan, A. Performance analysis and validation of an explicit local time-stepping algorithm for complex hypersonic flows. *Aerospace Science and Technology* **107**, 106321. doi: <https://doi.org/10.1016/j.ast.2020.106321> (2020).
45. Diwakar, A., Ramasahayam, V. & Bodi, K. Numerical Simulation of High-Enthalpy Flows at Thermochemical Equilibrium. *Journal of Thermophysics and Heat Transfer* **34**, 255–264. doi: <https://doi.org/10.2514/1.T5773> (2020).
46. Gottlieb, S. & Shu, C.-W. *Total Variation Diminishing Runge-Kutta schemes* tech. rep. 221 (Mathematics of computation of the American Mathematical Society, Jan. 1998), 73–85. doi: <https://doi.org/10.1090/S0025-5718-98-00913-2>.
47. Kennedy, C. A., Carpenter, M. H. & Lewis, R. Low-storage, explicit Runge–Kutta schemes for the compressible Navier–Stokes equations. *Applied Numerical Mathematics* **35**, 177–219. doi: [https://doi.org/10.1016/S0168-9274\(99\)00141-5](https://doi.org/10.1016/S0168-9274(99)00141-5) (2000).
48. Kronbichler, M. *The deal.II step-67 tutorial program* Accessed on April 19, 2022. [https://www.dealii.org/current/doxygen/deal.II/step\\_67.html](https://www.dealii.org/current/doxygen/deal.II/step_67.html).
49. Blazek, J. *Computational fluid dynamics: principles and applications* doi: <https://doi.org/10.1016/C2013-0-19038-1> (Butterworth-Heinemann, 2015).
50. Wang, Z. J., Fidkowski, K., Abgrall, R., Bassi, F., Caraeni, D., Cary, A., Deconinck, H., Hartmann, R., Hillewaert, K., Huynh, H. T., et al. High-order CFD methods: current status and perspective. *International Journal for Numerical Methods in Fluids* **72**, 811–845. doi: <https://doi.org/10.1002/fld.3767> (2013).
51. Arndt, D., Bangerth, W., Blais, B., Fehling, M., Gassmöller, R., Heister, T., Heltai, L., Köcher, U., Kronbichler, M., Maier, M., Munch, P., Pelteret, J.-P., Proell, S., Simon, K., Turcksin, B., Wells, D. & Zhang, J. The deal.II Library, Version 9.3. *Journal of Numerical Mathematics* **29**, 171–186. doi: <https://doi.org/10.1515/jnma-2021-0081> (2021).

52. Balay, S., Abhyankar, S., Adams, M. F., Benson, S., Brown, J., Brune, P., Buschelman, K., Constantinescu, E., Dalcin, L., Dener, A., Eijkhout, V., Gropp, W. D., Hapla, V., Isaac, T., Jolivet, P., Karpeev, D., Kaushik, D., Knepley, M. G., Kong, F., Kruger, S., May, D. A., McInnes, L. C., Mills, R. T., Mitchell, L., Munson, T., Roman, J. E., Rupp, K., Sanan, P., Sarich, J., Smith, B. F., Zampini, S., Zhang, H., Zhang, H. & Zhang, J. *PETSc/TAO Users Manual* tech. rep. ANL-21/39 - Revision 3.17 (Argonne National Laboratory, 2022).
53. Burstedde, C., Wilcox, L. C. & Ghattas, O. p4est: Scalable Algorithms for Parallel Adaptive Mesh Refinement on Forests of Octrees. *SIAM Journal on Scientific Computing* **33**, 1103–1133. doi: <https://doi.org/10.1137/100791634> (2011).
54. Geuzaine, C. & Remacle, J.-F. Gmsh: A 3-D finite element mesh generator with built-in pre-and post-processing facilities. *International Journal for Numerical Methods in Engineering* **79**, 1309–1331. doi: <https://doi.org/10.1002/nme.2579> (2009).
55. <https://www.salome-platform.org/>.
56. Ahrens, J., Geveci, B. & Law, C. Paraview: An end-user tool for large data visualization. *The visualization handbook* **717** (2005).
57. Young, A. D. Skin friction in the laminar boundary layer in compressible flow. *The Aeronautical Quarterly* **1**, 137–164. doi: <https://doi.org/10.1017/S0001925900000123> (1949).
58. Jacobs, P. A. *Single-block Navier-Stokes integrator* NASA Contractor Report ADA240385. <https://apps.dtic.mil/sti/citations/ADA240385>, accessed on July 14, 2022 (INSTITUTE FOR COMPUTER APPLICATIONS IN SCIENCE and ENGINEERING HAMPTON VA, 1991).
59. Degrez, G., Boccadoro, C. & Wendt, J. F. The interaction of an oblique shock wave with a laminar boundary layer revisited. An experimental and numerical study. *Journal of Fluid Mechanics* **177**, 247–263. doi: <https://doi.org/10.1017/S0022112087000946> (1987).
60. Boin, J.-P., Robinet, J. C., Corre, C. & Deniau, H. 3d steady and unsteady bifurcations in a shock-wave/laminar boundary layer interaction: a numerical study. *Theoretical and Computational Fluid Dynamics* **20**, 163–180. doi: <https://doi.org/10.1007/s00162-006-0016-z> (2006).
61. Lewis, J. E., Kubota, T. & Lees, L. Experimental investigation of supersonic laminar, two-dimensional boundary-layer separation in a compression corner with and without cooling. *AIAA Journal* **6**, 7–14. doi: <https://doi.org/10.2514/3.4434> (1968).
62. Carter, J. E. *Numerical solutions of the supersonic, laminar flow over a two-dimensional compression corner* in *Proceedings of the Third International Conference on Numerical Methods in Fluid Mechanics* (1973), 69–78.
63. Harvey, J., Holden, M. & Wadham, T. *Code Validation Study of Laminar Shock Boundary Layer and Shock/Shock Interactions in Hypersonic Flow Part B: Comparison with Navier-Stokes and DSMC Solutions* in *39th Aerospace Sciences Meeting and Exhibit* (2001). doi: <https://doi.org/10.2514/6.2001-1031>.
64. Holden, M. S. & Wadham, T. *Code Validation Study of Laminar Shock/Boundary Layer and Shock/Shock Interactions in Hypersonic Flow Part A: Experimental Measurements* in *39th AIAA Aerospace Sciences Meeting and Exhibit, Reno, NV, January* (2001), 8–12.
65. Gnoffo, P. A. *CFD validation studies for hypersonic flow prediction* in *39th Aerospace Sciences Meeting and Exhibit* (2001). doi: <https://doi.org/10.2514/6.2001-1025>.
66. Knight, D. *RTO WG 10-Test cases for CFD validation of hypersonic flight* in *40th AIAA Aerospace Sciences Meeting & Exhibit* (2002), 433. doi: <https://doi.org/10.2514/6.2002-433>.
67. Candler, G., Nompelis, I. & Druguet, M.-C. *Navier-Stokes Predictions of Hypersonic Double-Cone and Cylinder-Flare Flow Fields* in *39th Aerospace Sciences Meeting and Exhibit* (2001), 1024. doi: <https://doi.org/10.2514/6.2001-1024>.
68. Holden, M. & Moselle, J. Theoretical and experimental studies of the shock wave-boundary layer interaction on compression surfaces in hypersonic flow. *ARL 70-0002, Aerospace Research Laboratories, Wright-Patterson AFB, OH* (1970).
69. Rudy, D. H., Thomas, J. L., Kumar, A., Gnoffo, P. A. & Chakravarthy, S. R. Computation of laminar hypersonic compression-corner flows. *AIAA Journal* **29**, 1108–1113. doi: <https://doi.org/10.2514/3.10710> (1991).
70. Kitamura, K., Shima, E., Nakamura, Y. & Roe, P. L. Evaluation of Euler fluxes for hypersonic heating computations. *AIAA Journal* **48**, 763–776. doi: <https://doi.org/10.2514/1.41605> (2010).
71. Druguet, M.-C., Candler, G. V. & Nompelis, I. Effects of numerics on Navier-Stokes computations of hypersonic double-cone flows. *AIAA journal* **43**, 616–623. doi: <https://doi.org/10.2514/1.6190> (2005).

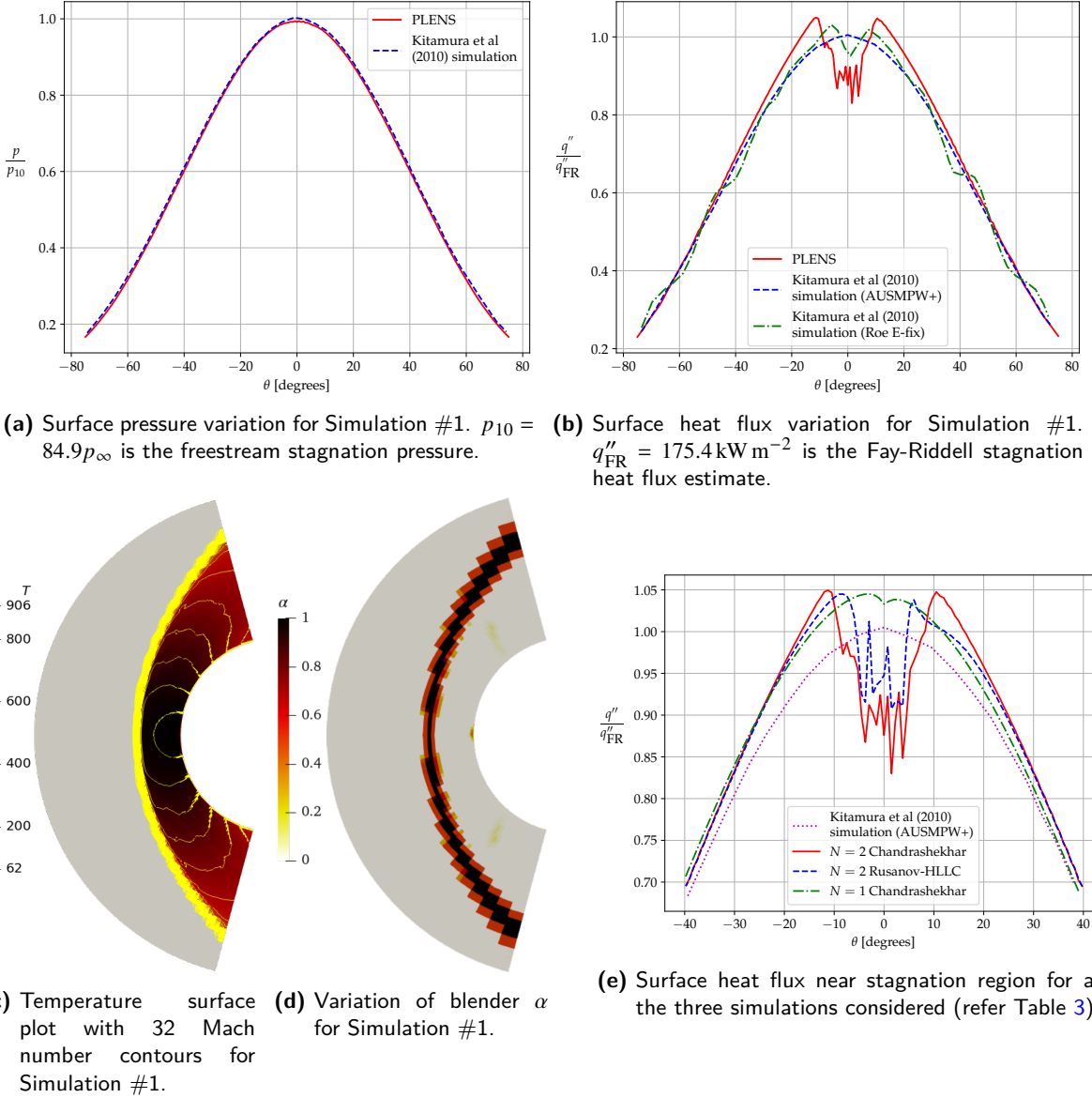


**Figure 15:** Numerical results obtained in Mach 8 flow over cylinder case proposed by Kitamura *et al.* [70]. Figures (a) to (d) show results using 2nd degree polynomial basis ( $N = 2$ ) with Chandrashekhar flux on  $100 \times 100$  grid with  $\Delta r_w = 0.4 \mu\text{m}$  (Simulation #1 in Table 3). In Figs. (a), (b) and (e), the result by Kitamura *et al.* [70] is from a FV numerical simulation.